

THE LOW TEMPERATURE THERMAL CONDUCTIVITY  
OF POTASSIUM ZINC FLUORIDE

By

MICHAEL WAYNE WOLF

Bachelor of Science  
Carroll College  
Waukesha, Wisconsin  
1964

Master of Science  
Northern Illinois University  
DeKalb, Illinois  
1967

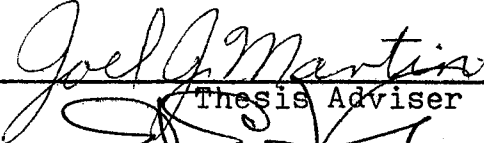
Submitted to the Faculty of the  
Graduate College of the  
Oklahoma State University  
in partial fulfillment of  
the requirements for  
the Degree of  
DOCTOR OF PHILOSOPHY  
July, 1974


THESIS  
1974D  
W854J  
cop.2

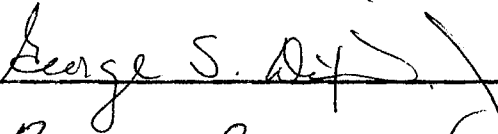
MAY 6 1975


THE LOW TEMPERATURE THERMAL CONDUCTIVITY  
OF POTASSIUM ZINC FLUORIDE


Thesis Approved:

  
\_\_\_\_\_  
Thesis Adviser

  
\_\_\_\_\_

  
\_\_\_\_\_

  
\_\_\_\_\_

  
\_\_\_\_\_  
Dean of the Graduate College

907125

## PREFACE

The study consisted of measuring the thermal conductivities of three undoped and two nickel-doped samples of potassium zinc fluoride which were grown by the author in the Oklahoma State University crystal-growing laboratory. Thermal conductivity measurements were taken on three different apparatuses, each providing data in a different temperature range from 0.42 to 200 K. The perovskite potassium zinc fluoride is a diamagnetic insulator which provides an ideal host lattice for the study of paramagnetic impurities and dopants. The results were analyzed in terms of the Debye-Callaway model which incorporated relaxation times resulting from boundary, isotope, and phonon-phonon scattering.

The author wishes to express his appreciation to his major adviser, Dr. Joel J. Martin, for his guidance and assistance throughout this study. Appreciation is also expressed to the other committee members, Dr. Elton E. Kohnke - Chairman, Dr. George S. Dixon, and Dr. Roger J. Schoepfel, for their assistance in the preparation of the final manuscript.

Finally, special thanks are expressed to my wife, Sandra, who proofread and typed the manuscript.

## TABLE OF CONTENTS

Chapter	Page
I. INTRODUCTION . . . . .	1
Purpose of Investigation . . . . .	1
Properties of Potassium Zinc Fluoride . . . . .	1
II. THEORY OF THE THERMAL CONDUCTIVITY OF INSULATORS . . . . .	6
Debye-Callaway Model . . . . .	10
Phonon Relaxation Times . . . . .	11
Lattice Thermal Conductivity Above the Thermal Conductivity Maximum . . . . .	24
III. EXPERIMENTAL PROCEDURE . . . . .	26
Growth Apparatus . . . . .	26
Growth Procedure . . . . .	28
Crystal Boule Descriptions . . . . .	31
Preparation of Samples . . . . .	32
Characterization . . . . .	33
Experimental Determination of Thermal Conductivity . . . . .	36
Sample Holders . . . . .	37
Thermometry . . . . .	51
Errors . . . . .	55
IV. RESULTS AND DISCUSSION . . . . .	69
Results . . . . .	69
Discussion . . . . .	72
Summary . . . . .	87
Future Work . . . . .	88
BIBLIOGRAPHY . . . . .	90
APPENDIX A - THE CALCULATION OF THE PARAMETERS $\Gamma$ OF EQUATION 12 FOR ISOTOPE POINT DEFECT SCATTERING IN $KZnF_3$ . . . . .	96
APPENDIX B - TABULATION OF DATA FOR SAMPLE NUMBER K1 ( $KZnF_3$ : UNDOPED) . . . . .	98

TABLE OF CONTENTS (continued)

APPENDIX C - TABULATION OF DATA FOR SAMPLE  
NUMBER K2 ( $KZnF_3$ : UNDOPED) . . . . . 99

APPENDIX D - TABULATION OF DATA FOR SAMPLE  
NUMBER K3 ( $KZnF_3$ : UNDOPED) . . . . . 101

APPENDIX E - TABULATION OF DATA FOR SAMPLE  
NUMBER KN1 ( $KZnF_3$ : NICKEL DOPED) . . . . . 103

APPENDIX F - TABULATION OF DATA FOR SAMPLE  
NUMBER KN2 ( $KZnF_3$ : NICKEL DOPED) . . . . . 105

APPENDIX G - ENERGY LEVEL DIAGRAM FOR  $Fe^{2+}(3d^6)$   
IN AN OCTAHEDRAL FIELD . . . . . 108

APPENDIX H - ENERGY LEVEL DIAGRAM FOR  $Ni^{2+}(3d^8)$   
IN AN OCTAHEDRAL FIELD . . . . . 109

## LIST OF TABLES

Table	Page
I. Dimensions of Samples . . . . .	34
II. Uncertainties in the Thermocouples . . . . .	60
III. Sensitivity and Resolution of Allen-Bradley Carbon Resistance Thermometers . . . . .	61
IV. Sensitivity and Resolution of Speer Carbon Resistance Thermometers . . . . .	63
V. Heat Loss Through Lead Wires . . . . .	65
VI. Estimated Radiation Heat Losses . . . . .	68
VII. Calculated Casimir Lengths for the Samples . . . . .	80
VIII. Parameters Used in the Debye-Callaway Integral . . . . .	83

## LIST OF FIGURES

Figure	Page
1. Crystal Structure of Potassium Zinc Fluoride . . .	3
2. The Oklahoma State University Bridgman-Stockbarger Apparatus . . . . .	27
3. Thermal Conductivity Sample Holder for 3 to 200 K	38
4. Thermal Conductivity Sample Holder for 1.2 to 4 K	42
5. Sample Clamps for Carbon Resistance Thermometers .	44
6. A. C. Bridge for Measurement of T in Thermal Conductivity Apparatus for 0.42 to 1.5 K . . . .	46
7. A. C. Bridge for Measurement of $\Delta T$ in Thermal Conductivity Apparatus for 0.42 to 1.5 K . . . .	47
8. Sample Chamber of the Cryostat for Thermal Conductivity Apparatus for 0.42 to 1.5 K . . . .	48
9. Helium III Cryostat with Associated Equipment for Thermal Conductivity Apparatus for 0.42 to 1.5 K	49
10. Thermal Conductivity of Undoped Potassium Zinc Fluoride . . . . .	70
11. Low Temperature Thermal Conductivity Data of Undoped and Nickel-Doped Potassium Zinc Fluoride	71
12. Thermal Conductivity of Nickel-Doped Potassium Zinc Fluoride . . . . .	73
13. Thermal Conductivity of Related Perovskites . . .	74
14. Theoretical Curves of Potassium Zinc Fluoride Calculated by the Debye-Callaway Theory . . . .	81
15. Plot of $\lambda/T^3$ vs. T . . . . .	86



## CHAPTER I

### INTRODUCTION

#### Purpose of Investigation

The diamagnetic perovskite potassium zinc fluoride is an inorganic fluoride compound that has received very little attention; therefore, many of its properties are unknown or unconfirmed. For a better understanding of its physical properties, the thermal conductivities of undoped and nickel-doped potassium zinc fluoride were measured over a wide temperature range. These measurements provided a means of studying the phonon-scattering mechanisms predominant in undoped and doped single crystals of potassium zinc fluoride. Because it is diamagnetic and has a high order of symmetry, potassium zinc fluoride makes an excellent host lattice in which paramagnetic ions can be substituted for the zinc ions, thus providing a means of studying the spin-phonon interaction by thermal conductivity measurements. The results of these measurements were analyzed using the Debye-Callaway model.

#### Properties of Potassium Zinc Fluoride

A method that has been used successfully for growing potassium zinc fluoride and the one by which the samples in

this study were grown is the Bridgman-Stockbarger method in which a stoichiometric mixture of potassium fluoride and zinc fluoride is combined at a high temperature. This and other methods have been used successfully for synthesizing potassium zinc fluoride (1-12). Since potassium zinc fluoride is an "allowed perovskite" according to the tolerance factor formula (8-12), methods and techniques used for other potassium metal fluorides should produce single crystals (13-23).

Recent x-ray crystallographic studies (1-5, 8, 9, 24) show that potassium zinc fluoride has a cubic perovskite structure with one molecule per unit cell and a lattice constant of  $4.054\text{\AA}$  (24). This structure is shown in Figure 1. It has a symmetry space group of  $O_h^1$ ,  $pm\bar{3}m$ . However, some earlier studies (10, 11) claim a tetragonal structure, which appears to be an erroneous conclusion, possibly because of sample impurities or distortions in the lattice as a result of synthesizing techniques.

The elastic constants  $C_{11}$ ,  $C_{12}$ , and  $C_{44}$  have been determined (24) from the room temperature velocity of sound measurements. The calculated elastic constants are

$$C_{11} = (13.45 \pm 0.05) \times 10^{11} \text{ dynes/cm}^2$$

$$C_{12} = (5.27 \pm 0.05) \times 10^{11} \text{ dynes/cm}^2$$

$$C_{44} = (3.81 \pm 0.02) \times 10^{11} \text{ dynes/cm}^2$$

using a density of  $4.024 \pm 0.001$  grams per cubic centimeter. Gesland et al. (24) also calculated an adiabatic compressibility of  $(1.25 \pm 0.02) \times 10^{-12} \text{ cm}^2/\text{dyne}$  and an anisotropic

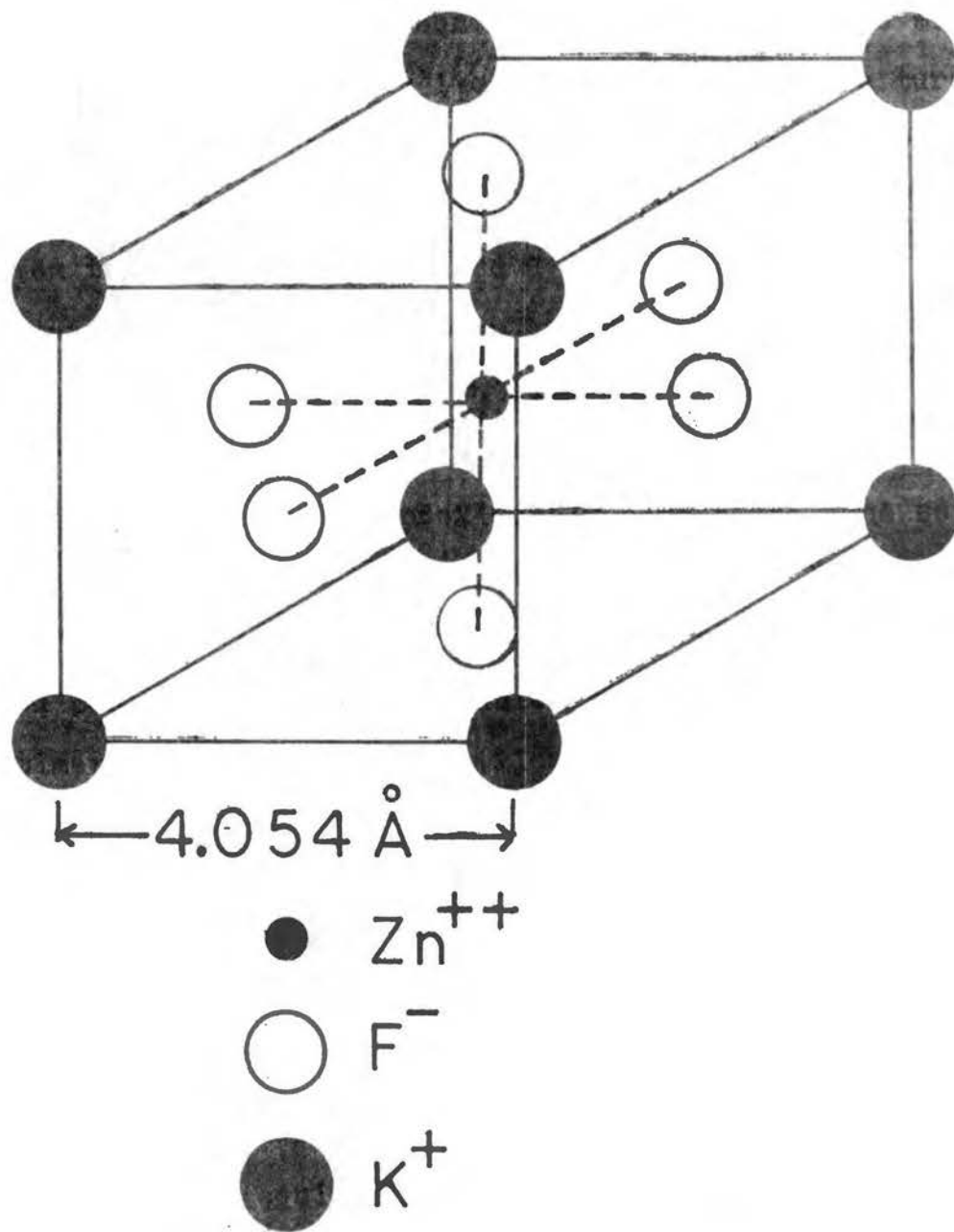


Figure 1. Crystal Structure of Potassium Zinc Fluoride

parameter of  $0.93 \pm 0.02$ .

Because pure potassium zinc fluoride is diamagnetic, it is suitable as a base material for doping with magnetic ions at various concentrations. These magnetic ions are substituted into the lattice in place of the zinc ions during growth; and if the tolerance factor is favorable, this substitution can be made in any proportion. The two dopants studied to date in potassium zinc fluoride are nickel (3, 4) and manganese (10, 12, 25-27). More intensive studies of magnetic ion doping have been in the related compound potassium magnesium fluoride where transition metal ions (28, 29) and rare-earth ions (13) have been used. Paramagnetic color center defects have also been produced in potassium magnesium fluoride by irradiation (30, 32).

Electron paramagnetic resonance is an important tool in identifying the magnetic impurities in nonmagnetic host lattices and was one of the methods used to characterize the samples in this research. The electron paramagnetic resonance of potassium magnesium fluoride, which has magnetic and physical properties similar to those of potassium zinc fluoride, doped with various magnetic impurities has been measured extensively (13, 19, 33); but the only reported work on potassium zinc fluoride is by Kappers and Halliburton (34).

Optical absorption studies on undoped and doped potassium zinc fluoride have been carried out in detail

(8, 35). This was another method used for characterizing the samples. Because of the use of magnesium-doped potassium zinc fluoride in cathode ray tubes, considerable information is available about its fluorescence (10, 12, 35).

CHAPTER II  
THEORY OF THE THERMAL CONDUCTIVITY  
OF INSULATORS

In an electrically insulating dielectric crystal, the heat is transported by elastic waves or phonons. If the phonon distribution is not in equilibrium throughout the solid, a net flow of heat results, giving rise to thermal conduction. An exact calculation of the thermal conductivity,  $\lambda$ , in a crystal lattice would be theoretically possible if the entire phonon spectrum and the anharmonicity of the lattice forces of the crystal were completely known in detail. Although the phonon spectrum is known for many materials, there is very little known about the lattice force anharmonicity. Therefore, a theoretical calculation of the lattice thermal conductivity which would give exact results is impossible. As a result, numerous models have been developed for calculating approximate values to explain quantitatively the experimental data. Reviews of the theory of thermal conductivity in solids have been given by Klemens (36, 37) and Carruthers (38).

The first realistic expression for the thermal conductivity in a solid was derived by Debye (39). After assuming a "phonon gas," one can derive an expression for

the thermal conductivity,  $\lambda$ , by making an analogy to the kinetic theory of gases, giving

$$\lambda = \frac{1}{3} C v \ell \quad [1-a]$$

or, using  $\ell = v\tau$ ,

$$\lambda = \frac{1}{3} C v^2 \tau \quad [1-b]$$

where  $C$  is the specific heat of the material,  $v$  is the velocity of sound in the material,  $\ell$  is the phonon mean-free-path, and  $\tau$  is the phonon relaxation time between the various scattering processes. One of the assumptions made in the derivation of Equations [1-a] or [1-b] is that the heat is flowing through a perfect crystal that is infinitely long with ideally rough walls. Also, all the phonons are characterized by one frequency.

In 1929, Peierls (40) gave the first rigorous treatment of thermal conductivity by quantizing the lattice waves to include the entire phonon spectrum which transports the heat. A summation over all normal modes is taken, giving

$$\lambda = \frac{1}{3} \sum_{\omega} C(\omega) v^2 \tau(\omega) \quad [2]$$

where the index  $\omega$  is the phonon frequency. Klemens (36, 37) derived an integral form of Equation [2].

$$\lambda = \frac{1}{3} \int C(\omega) v^2 \tau(\omega) d\omega \quad [3]$$

Assuming that the phonon spectrum can be characterized by a Debye distribution of limiting frequency  $\omega_D$  and using the definition of the specific heat, Equation [3] can be put into the form

$$\lambda = \frac{1}{2\pi^2 v} \int_0^{\omega_D} \tau \frac{\hbar^2 \omega^4}{kT^2} \frac{e^{\hbar\omega/kT}}{(e^{\hbar\omega/kT} - 1)^2} d\omega \quad [4]$$

where  $k$  is the Boltzmann constant and  $\hbar$  is Planck's constant divided by  $2\pi$ . In using the Debye model given above, various assumptions are made. First, it is assumed that a Debye-like phonon spectrum can be used. Through the use of an appropriate average value, this assumption neglects the effects of dispersion and anisotropy. Also, an average velocity of sound, which is constant for all frequencies and temperatures, is assumed. Polarization is not considered as a factor entering into the calculations.

The major problem in solving Equation [4] for a particular material is determining what form of relaxation time should be used. There is no one form of the relaxation time that can be used for all materials at all temperatures. The relaxation time,  $\tau$ , depends upon each scattering mechanism present in the material, and the mechanism which is predominant at one temperature may be an insignificant scattering mechanism at a different temperature. Any physical or chemical impurity or imperfection in the crystal lattice will change the phonon distribution by acting as a scattering mechanism and will, in turn, greatly affect the thermal conductivity, which is dependent upon the predominant relaxation time for the temperature under consideration. Some of the dominant scattering mechanisms are boundary, point defect, umklapp,



dislocation, and resonant scattering. These processes are all characterized as nonmomentum-conserving processes; therefore, they can result in a net resistance to the flow of heat within a material.

Klemens (41, 42) argued that each scattering process is completely independent of the others; therefore, by using individual relaxation times, he calculated separately the thermal conductivity resulting from each process. This greatly reduced the mathematical difficulties in solving Equation [3]. Thus, one can determine the thermal resistivity resulting from each scattering mechanism by taking the inverse of its thermal conductivity, which was calculated from Equation [3]. The total thermal resistivity would then be the sum of the contributions resulting from each scattering mechanism. The total thermal conductivity is then the inverse of the total thermal resistivity. The resultant calculated thermal conductivity in many cases does not correspond accurately to the experimental data for large temperature ranges. The primary problem with this theory is that although the scattering mechanisms are independent, each relaxation time has a different frequency dependence which can change the phonon spectrum in a particular manner. If this change in the phonon spectrum is not considered in the thermal conductivity integral for the other scattering mechanisms, then the calculated thermal conductivity will be too high. Assuming temperatures much below the Debye temperature,  $T \ll \theta_D$ , Klemens derived the thermal conductivity

integral for each of the most dominant scattering mechanisms.

### Debye-Callaway Model

A more mathematically rigorous approach to deriving a thermal conductivity relation is to begin with the Boltzmann transport equation (36, 42-45). In the derivation, an integral equation is derived which must be approximated. The two standard approaches are either to use trial functions in conjunction with the variational principle or to use a relaxation time concept. The more common approach has been the relaxation time model developed by Callaway (45), which has been successful to explain phenomenologically the low temperature thermal conductivity data. The resulting thermal conductivity integral is

$$\lambda = \frac{k}{2\pi^2 v} \left( \frac{kT}{\hbar} \right)^3 \left[ \int_0^{\frac{\theta}{T}} \tau_c \frac{x^4 e^x}{(e^x - 1)^2} dx + B \int_0^{\frac{\theta}{T}} \frac{\tau_c}{\tau_N} x^4 \frac{e^x}{(e^x - 1)^2} dx \right] \quad [5]$$

where

$$B = \frac{\int_0^{\frac{\theta}{T}} \frac{\tau_c}{\tau_N} \frac{x^4 e^x}{(e^x - 1)^2} dx}{\int_0^{\frac{\theta}{T}} \frac{1}{\tau_N} \left[ 1 - \frac{\tau_c}{\tau_N} \right] \frac{x^4 e^x}{(e^x - 1)^2} dx}$$

and

$$x = \frac{\hbar\omega}{kT}$$

$\theta$  is the Debye limiting temperature,  $\tau_N$  is the relaxation time resulting from the normal processes which indirectly add to the thermal resistance, and  $\tau_c$  is a combined relaxa-

tion time found by the reciprocal addition of the relaxation times for all the different scattering mechanisms. The second integral in Equation [5] results from the inclusion of the nonresistive normal processes in the total effective relaxation time,  $\tau_c$ . This term adjusts for the underestimate in the thermal conductivity calculated in the first term. This adjustment, which results from consideration of the normal processes, accounts for less than ten percent of the calculated thermal conductivity at 200 K, and its effect decreases rapidly as the temperature decreases; therefore, this term is omitted in the present calculations. The major contribution of Callaway's treatment is the reciprocal addition of all the relaxation times to get one total relaxation time  $\tau_c$ .

$$\tau_c^{-1} = \sum_i \tau_i^{-1} \quad [6]$$

### Phonon Relaxation Times

#### Boundary Scattering

As the temperature of the crystal decreases, the importance of the long wavelength phonons increases. The phonon mean-free-path cannot increase without limit because the thermal conductivity decreases as the result of collisions with the crystal's walls; therefore, below the thermal conductivity maximum, the long-wavelength phonons begin scattering off the crystal's boundaries and become the dominating factor in the thermal conductivity of the crys-

tal. Casimir (46) first derived the relaxation time resulting from diffuse boundary scattering as

$$\tau_B^{-1} = \frac{v}{L} \quad [7]$$

where  $v$  is the velocity of sound in the crystal and  $L$  is an effective sample diameter which is dependent upon the sample's geometry and surface roughness. For a "perfectly rough" and rectangular sample,

$$L = 2\pi^{-\frac{1}{2}}(l_1 l_2)^{\frac{1}{2}} \quad [8]$$

where  $l_1$  and  $l_2$  are the dimensions of the sample's cross section perpendicular to the heat flow with the assumption that the crystal is long compared to either  $l_1$  or  $l_2$ . If the sample is not "perfectly rough," specular reflections of the phonons occur which increase the phonon mean-free-path, resulting in an increase of the measured thermal conductivity. Berman et al. (47) have defined a "roughness" factor and have experimentally verified Casimir's relation for various "roughnesses" of the sample's surface. A "perfectly rough" surface can be obtained from chemical etching, sand blasting, or using sandpaper, giving a roughness factor of unity. If the sample's length is of the order of its other dimensions, then a correction for reflection off the crystal's ends must be made (47). At low enough temperatures, when all the phonon mean-free-paths are comparable to the sample's cross-sectional dimensions, the relaxation time is usually entirely limited by the boundary scattering, which is temperature and frequency independent.

The thermal conductivity curve for these temperatures will have a slope of  $T^3$  resulting from the temperature dependence of the specific heat.

Other scattering mechanisms are known which also give a  $T^3$  dependence at low temperatures, such as grain boundaries (48), bubbles (49), clusters (50), colloids (51-53), mosaic substructures (54), and possibly certain types of magnetic impurity scattering (55-57).

### Point Defect Scattering

The chemical impurities and physical imperfections in the crystal lattice have a major effect in determining the height and shape of the thermal conductivity curve. If the defects have an effective diameter which is small compared to the phonon wavelength, they are classified as point defects. A point defect affects the thermal conductivity because it disturbs the periodicity of the lattice in three ways: the defect will have a different mass than the atoms of the host lattice; there will be a change in the force constants; and there will be a change in the nearest neighbor distance (41). Point defects, if randomly distributed, result in a Rayleigh-type scattering of the phonons. Klemens found that the form of the relaxation time is

$$\tau_{PD}^{-1} = A\omega^4 \quad [9] \quad \text{where } A = \frac{\delta^3 \Gamma}{4\pi v^2}. \quad [10]$$

Various forms of  $\Gamma$  have been suggested (37, 38), one of

which is (58)

$$\Gamma = \sum_i x_i \left\{ \left( \frac{\Delta M_i}{M} \right)^2 + 2 \left[ \left( \frac{\Delta f_i}{f} \right) - 8.4 \left( \frac{\Delta R_i}{R} \right) \right]^2 \right\} \quad [11]$$

where  $\delta$  is the cube root of the atomic volume;  $v$  is the velocity of sound in the material;  $x_i$  is the fractional concentration of the  $i^{\text{th}}$  impurity;  $\Delta M_i$  is the difference between the atomic mass of the  $i^{\text{th}}$  point defect and the average atomic mass,  $M$ , of the lattice;  $\Delta f_i$  is the difference in the force constants with  $f_i$  the force constant for the  $i^{\text{th}}$  point defect and  $f$  the force constant for the lattice atoms;  $\Delta R_i$  is the difference between the nearest neighbor distance of the  $i^{\text{th}}$  defect and the nearest neighbor distance of the lattice atoms,  $R$ ; and  $\gamma$  is the Grüneisen anharmonicity parameter. An exact calculation of  $\Gamma$  is impossible since detailed knowledge of the force constants and the anharmonicity of the lattice are not known. The first term in Equation [11] involving mass difference can, however, be approximated for the case of isotope point defects. Pomeranchuk (59), using perturbation theory, was the first to attempt to calculate the effect of the scattering of the phonons by the variation in the mass as the result of isotopes in the lattice. Klemens (41) modified Pomeranchuk's result by a numerical constant. Carruthers (38) and Klein (60) also contributed modifications to the form of the point defect scattering relation. Slack (61) modified Klemens' result so that it may be applied to compounds containing isotopes of many elements.

For a compound with the general form  $A_x B_y C_z \dots$ , the form of Equations [9] and [10] still holds, but the form of the first term in Equation [11] becomes

$$\Gamma = \Sigma \frac{x}{x+y+z+\dots} \left( \frac{M_A}{\bar{M}} \right)^2 \Gamma_A + \frac{y}{x+y+z+\dots} \left( \frac{M_B}{\bar{M}} \right) \Gamma_B + \dots [12]$$

where

$$\Gamma_A = \Sigma_i f_i \left( \frac{\Delta M_i}{\bar{M}_A} \right)^2 \dots \dots [13]$$

$M_A$  and  $M_B$  are the masses of the isotopes of the atoms of types A and B respectively,  $\bar{M}_A$  and  $\bar{M}_B$  are the average masses of these atoms, and  $\bar{M}$  is the average molecular mass defined as

$$\bar{M} = \frac{x\bar{M}_A + y\bar{M}_B + \dots}{x + y + \dots} [14]$$

The relaxation time calculated for Rayleigh scattering from point defects, as determined by Equations [9], [10], and [12], when added to the various other appropriate relaxation times will always give larger calculated thermal conductivities in the maximum region than would be experimentally determined; however, the results are qualitatively correct and give good estimates. If precise fits are required, then the coefficient A is increased until a phenomenological "fit" is obtained. This relaxation time is strongly frequency dependent and is temperature independent. This affects primarily the peak region; the more point defects present, the lower the peak thermal conductivity becomes. This lowering is approximately symmetrical about the thermal

conductivity maximum and disappears at both the lower and the higher temperatures.

### Phonon-Phonon Scattering

Above the thermal conductivity maximum, the effects resulting from the physical and chemical imperfections in the crystal lattice become less effective in influencing the shape of the thermal conductivity curve. The dominating processes become the phonon-phonon interactions. For the three phonon-scattering processes, the phonon-phonon relaxation time can be treated theoretically with reasonable accuracy only for the very simplest special cases. The mathematical calculations are extremely difficult even for the special cases in which the detailed phonon spectrum is known. Therefore, a phenomenological relaxation time is usually employed for representing an average phonon scattering. As a result, many different forms representing the relaxation time have been suggested.

For umklapp phonon-phonon interactions, u-processes, Callaway (45) used the form

$$\tau_U^{-1} = B_1 T^3 \omega^2 e^{-\theta/aT} \quad [15]$$

where  $a$  is a constant integer, usually about 2, which depends on the dispersion in the vibrational spectrum of the material and  $B_1$  is a fitted parameter. Another form used by Berman and Brock (62) is

$$\tau_U^{-1} = B_1 T^2 \omega^2 e^{-\theta/aT}. \quad [16]$$



Klemens has used various forms (36)

$$\tau_U^{-1} = B_1 T^3 \omega^2 e^{-\theta/aT} \quad [17]$$

$$\tau_U^{-1} = B_1 T^3 \omega e^{-\theta/aT} \quad [18]$$

and in the long wavelength limit

$$\tau_U^{-1} = B_1 T \omega \quad \text{for } T > \theta \quad [19]$$

$$\tau_U^{-1} = B_1 T^{-1} \omega e^{-\theta/aT} \quad \text{for } T \ll \theta \quad [20]$$

and for high temperature (36)

$$\tau_U^{-1} = B_1 T \omega^2. \quad [21]$$

The form that "fits" the data presented in the present work was originally obtained semi-empirically by Slack and Galginaitis (63):

$$\tau_U^{-1} = B_1 T \omega^2 e^{-\theta/aT}. \quad [22]$$

Although  $B_1$  will be determined using a computer curve fit of the experimental data, Slack and Galginaitis (22) give the semi-empirical expression with  $B_1$  as

$$B_1 = \frac{\hbar \gamma^2}{m_a v^2 \theta} \quad [23]$$

where  $m_a$  is the average mass of a single atom in the solid. At high temperatures where the umklapp processes are predominant, the thermal conductivity curve usually follows a  $T^{-1}$  dependence.

The three phonon normal processes are the only phonon-

phonon interactions which conserve momentum. They cannot cause a thermal resistance directly, but they do influence the thermal conductivity by transferring momentum from one part of the frequency distribution to other frequency modes which have already been depleted by isotope scattering (64). Thus, additional phonons are available to be scattered by the impurities, resulting in a lowering of thermal conductivity in the peak region where isotope scattering is predominant. The effect of the normal processes on the thermal conductivity is a formidable theoretical problem. To incorporate a relaxation time resulting from normal processes into Callaway's theory, one must determine its form on a phenomenological basis. However, Herring (65) has given some semi-empirical arguments as to the various forms which could be used for various conditions and different types of phonons, longitudinal or transverse, and for the various temperature ranges. Holland (66) gives a list of some of the forms used. The form which fits the data in the present calculations is

$$\tau_N^{-1} = B_2 T \omega^2 \quad [24]$$

where  $B_2$  is a "fitted" parameter. The total relaxation time as a result of three phonon-scattering processes is

$$\tau_{PP}^{-1} = \tau_U^{-1} + \tau_N^{-1}. \quad [25]$$

### Dislocation Scattering

If the crystal lattice has a substantial number of

dislocations, an additional relaxation time must be considered for explaining the experimental data. The general form for the dislocation relaxation time is

$$\tau_D^{-1} = Y\omega \quad [26]$$

where  $Y$  is a constant which is proportional to the dislocation density. Three authors, Klemens (36), Carruthers (38), and Ohashi (67), have developed empirical relations for the form of  $Y$ . From a "fit" of the experimental data, an estimate of the dislocation density can be obtained. The temperature dependence of the thermal conductivity, which is characteristic of dislocation scattering, is a  $T^2$  dependence between the low temperature side of the peak to the region where boundary scattering becomes predominant.

### Resonant Scattering

When the phonon energy is equal to the interlevel spacing of a system, such as paramagnetic ions in a non-magnetic host lattice, a resonant scattering of the phonons may occur. One result of this type of scattering is the production of an indentation or dip in the thermal conductivity curve which has a resonance frequency  $\omega_D$  associated with it. One empirical form of the resonant relaxation time suggested by Pohl (68) to fit his thermal conductivity data on potassium chloride containing small concentrations of potassium nitrite is

$$\tau_r^{-1} = \frac{A_r \omega^2}{(\omega_0^2 - \omega^2)^2 + \left(\frac{\Delta}{\pi}\right)^2 \omega^2 \omega_0^2} \quad [27]$$

where  $A_r$  is a fitted parameter and  $\Lambda$  describes the damping. This temperature independent form gives good fits to the thermal conductivity having dips below the maximum; this usually occurs for polyatomic impurity centers. For dips above the maximum, Walker and Pohl (57) used the form

$$\tau_r^{-1} = \frac{A_r T^2 \omega^2}{(\omega_0^2 - \omega^2)^2 + \left(\frac{\Delta}{\pi}\right)^2 \omega_0^2 \omega^2} \quad [28]$$

which is temperature dependent. This form is usually required for monoatomic impurity centers. Variations (57) of Equations [27] and [28] are

$$\tau_r^{-1} = \frac{A_r \omega^2}{(\omega_0^2 - \omega^2)^2} \quad \text{and} \quad \tau_r^{-1} = \frac{A_r T^2 \omega^2}{(\omega_0^2 - \omega^2)^2} \quad [29]$$

### Spin-Lattice Relaxation

In paramagnetic non-Kramers ions, it is possible to have a spin-lattice relaxation process. Two possible mechanisms are the "direct" process and the Raman process. In the "direct" process, a single phonon of energy equivalent to that of the splitting between the spin state of the ion is absorbed and subsequently re-emitted in an arbitrary direction, resulting in an increase in the thermal resistance. For this process to have any considerable effect on the thermal conductivity, the splitting energy,  $k\Delta$ , with  $\Delta$  expressed in Kelvins, must be such that it absorbs the dominant heat-carrying phonons. For small splittings, the thermal resistance resulting from direct processes will become important at very low temperatures.

If there is phonon scattering as a result of phonon-induced transitions between the two levels  $|a\rangle$  and  $|b\rangle$  of a non-Kramers ion, then the relaxation time which must be added to those previously given is (69)

$$\tau_d^{-1} = \frac{\pi}{\hbar} \left| \langle a | V_0 | b \rangle \right|^2 \frac{\omega}{\rho v^2} g(\omega - \omega_0) \Delta N_S \quad [30]$$

where  $\rho$  is the density,  $g(\omega - \omega_0)$  is the line-shape function for the spin packet,  $\Delta N_S$  is the spin population difference per unit volume between the two states considered,  $\hbar\omega_0$  is the energy separation between the states, and  $V_0$  is the coupling operator. Summing over all the possible transitions between the ground state and the excited multiplets and summing over all the spins present will give a total phonon relaxation time resulting from direct processes. Morton and Lewis (70) give the results as

$$\tau_d^{-1} = \frac{\pi}{\hbar \rho v^2} \int \Sigma \left| \langle a | V_0 | b \rangle \right|^2 \omega N_S g_t(\omega - \omega_0) \times f'(\omega_{ot} - \bar{\omega}_{ot}) F(\omega_{ot}, T) d\omega_{ot} \quad [31]$$

where the suffix  $t$  is the index which represents the  $t^{\text{th}}$  multiplet,  $f'(\omega_{ot} - \bar{\omega}_{ot})$  is the fraction of spins which can possibly have a transition to another state, and

$$F(\omega_{ot}, T) = \frac{1 - \exp(-\hbar\omega_{ot}/kT)}{3 - 5 \exp(-\hbar\omega_{ot}/kT)} \quad [32]$$

is the population difference factor. For frequencies  $\omega \ll kT/\hbar$ , Equation [31] is frequency independent. Fox et al. (71), making the approximation of the frequency times the relaxation time for thermal equilibrium to be established

with the ground state, derived a form for Equation [30] of

$$\tau_d^{-1} = \frac{v}{L} \left[ 1 + \frac{A_d \tau_0}{2T} \coth \left( \frac{T_0}{2T} \right) \frac{1}{2 + \exp(T_0/T)} \right] \quad [33]$$

where  $L$  is the mean-free-path resulting from boundary scattering,  $T_0$  describes the separation of the multiplet from the ground state, and  $A_d$  is a proportionality constant.

Another form for the relaxation time for spin-phonon interactions associated with direct processes is given by Fox et al. (72)

$$\tau_d^{-1} = \left( \frac{NA_d}{v} \right) \left[ \frac{\omega \tau_{\text{Level}}}{T (1 + \omega^2 \tau_{\text{Level}}^2)} \right] \quad [34]$$

where  $N$  is the magnetic impurity concentration,  $A_d$  is a proportionality constant, and  $\tau_{\text{Level}}$  is the spin-lattice relaxation time for the multiplet levels. For direct processes,  $\tau_{\text{Level}}^{-1}$  is proportional to  $T$ , making  $\tau_d$  independent of temperature and frequency, which will result in the thermal conductivity's having the boundary scattering type dependence of  $T^3$ .

The Raman process is a two-phonon process where the initial phonon energy is larger than that of the level splitting. A portion of the initial phonon's energy is absorbed, leaving a phonon of lower energy. A phonon of energy equal to that of the level splitting is then re-emitted in a random direction. This process involves all the phonons in the phonon spectrum of energy larger

than  $k\Delta$ . If the splitting energy,  $k\Delta$ , is much less than  $kT$ , the energy of the most abundant phonons, then the Raman process will be dominant over the "direct" process. Orbach (73) gives the phonon relaxation time of

$$\tau_R^{-1} = \frac{S^4 \Gamma_c^2 N_v}{12\pi \rho v^7} \omega^2 \left[ \omega^2 + \left( \frac{k\Delta}{h} \right)^2 \right] \quad [35]$$

where  $S$  is the spin value of the magnetic ion,  $\Gamma_c$  is a phenomenological coupling constant, and  $N_v$  is the number of spin impurities per unit volume. At high temperatures, the relaxation time is proportional to  $\omega^4$ , which results in a scattering with the same frequency and temperature dependence as point defect scattering.

### Dipole Scattering

Another phonon-scattering mechanism which must be considered in some cases is scattering by dislocation dipoles which, at low temperatures, lowers the thermal conductivity. Moss (74) gives the form of the relaxation time as

$$\tau_{DD}^{-1} = \tau_D^{-1} \sin^2 \theta / \frac{\vec{k} \cdot \vec{d}}{2} \quad [36]$$

where  $\tau_D$  is the relaxation time resulting from dislocation scattering and  $\vec{d}$  is the vector joining two dislocations. The temperature dependence of the thermal conductivity resulting from dipole scattering is proportional to  $T$ .

### Combined Relaxation Time

When using Equation [5] to obtain a computer fit of the thermal conductivity experimental data from room tem-

perature down to liquid helium temperature, the relaxation times for boundary, isotope, and phonon-phonon scattering must always be included in the total relaxation time.

Other relaxation times, as already discussed, may be required depending on the chemical and physical impurities and imperfections present. The shape of the curve will indicate which additional relaxation times are needed.

The form of Equation [6] will be

$$\tau_{\text{Combined}}^{-1} = \tau_{\text{Boundary}}^{-1} + \tau_{\text{Isotope}}^{-1} + \tau_{\text{Phonon-Phonon}}^{-1} + \sum_{\text{All Others}} \tau^{-1} \quad [37]$$

#### Lattice Thermal Conductivity Above the Thermal Conductivity Maximum

For temperatures above the thermal conductivity maximum where the thermal conductivity is proportional to  $T^{-1}$ , the only important scattering mechanism is the phonon-phonon interactions. Leibfried and Schlömann (75) developed a model for treating the acoustical-acoustical three-phonon scattering in terms of the thermal resistance resulting from anharmonic terms in the three-phonon interactions. The Leibfried and Schlömann relation was modified by Julian (76), who made a correction in the numerical coefficient, and by Steigmeier and Kudman (77), who modified the form by replacing the Grüneisen parameter,  $\gamma$ , with  $(\gamma + 0.5)$ . Roufosse and Klemens (78) reformulated the Leibfried and Schlömann relation for a lattice with one



atom per unit cell and obtained the same relation for the thermal resistivity only a factor of  $6.8^4$  larger. The resulting thermal conductivity relation is

$$\lambda = \frac{3^{1/3}}{2^{1/6} \pi^{4/3} \gamma^2} \frac{k^3}{h^3} M a \theta^2 \frac{\theta}{T} \quad [38-a]$$

where  $a$  is the lattice constant,  $M$  is the mass of a unit cell, and  $\theta$  is the Debye temperature. The Debye temperature can be calculated by the relation

$$\theta = \frac{\hbar v}{k} \frac{v}{V} (6\pi^2)^{1/3} \quad [38-b]$$

where  $v$  is the average sound velocity within the crystal and  $V$  is the volume of a unit cell. The average sound velocity is calculated by averaging the transverse ( $v_t$ ) and longitudinal ( $v_l$ ) sound velocities using the equation

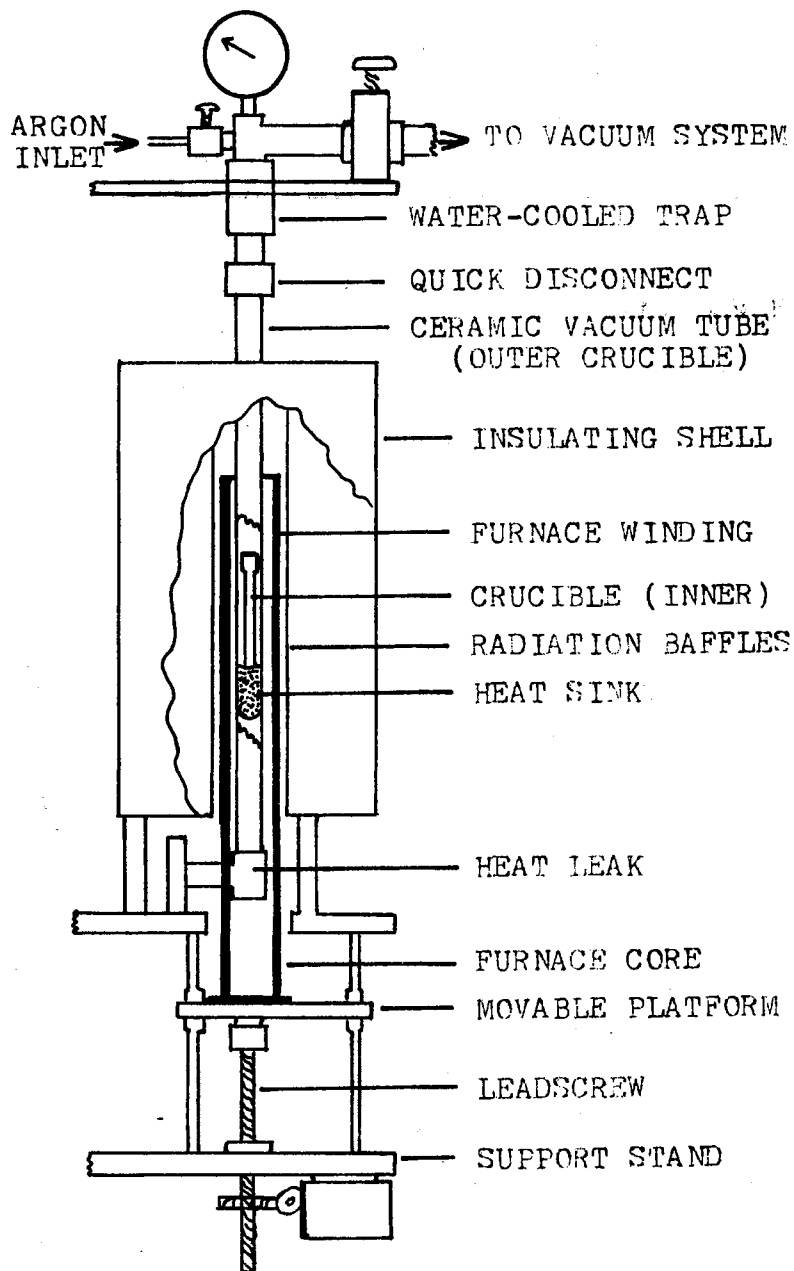
$$\frac{1}{v} = \frac{1}{3} \left( \frac{2}{v_t} + \frac{1}{v_l} \right). \quad [38-c]$$

## CHAPTER III

### EXPERIMENTAL PROCEDURE

#### Growth Apparatus

The undoped and nickel-doped samples of potassium zinc fluoride used in this study were grown in the Oklahoma State University crystal-growth laboratory by a modified Bridgman-Stockbarger method. The basic principles of this method were developed by Bridgman (79) and refined by Stockbarger (80, 81). Figure 2 is a schematic of the main components of the Oklahoma State University apparatus: inner crucible, outer crucible, furnace, heat sink, and a method of controlling the growing environment. The crystal boule was grown in a high-purity graphite inner crucible. The outer crucible was a ceramic tube of Coors Mullite and was used to enclose the graphite crucible. By using the valves indicated in Figure 2, one could control the crystal's environment. Also shown is a compound Bourdon tube pressure gauge which monitored the pressure up to two atmospheres above and one atmosphere below atmospheric pressure. A quick disconnect fitting connected the ceramic tube to the argon gas and pumping systems. This quick disconnect fitting also served as a safety feature in that if the pressure inside the ceramic tube increased over two



Source: 82

Figure 2. The Oklahoma State University  
Bridgman-Stockbarger  
Apparatus

atmospheres, the vacuum system was lifted off the tube and the pressure was released. Initially the furnace was in its lowest position when the bottom of the inner crucible was in the hottest region. This furnace was constructed so that it could rise at a constant speed sweeping a large temperature gradient of 20 to 50 degrees per centimeter from the lowest portion of the inner crucible to the highest. The heat sink was a solid piece of graphite which thermally connected the bottom of the inner crucible to the inner wall of the ceramic tube. The closed end of the outer crucible was then placed into thermal contact with a heat leak which removed the heat of solidification from the system, thus giving the proper temperature gradient within the crucible during growth (82). C. T. Butler (82) gives a detailed discussion of the Oklahoma State University Bridgman-Stockbarger apparatus and a summary of the growth theory.

#### Growth Procedure

The procedure developed for growing the large single crystals of undoped and doped potassium zinc fluoride used in this study is substantially different from the one previously employed at Oklahoma State University. The previous procedure resulted in small crystal boules that contained large bubbles throughout. These types of samples are unacceptable for thermal conductivity studies, which require large, pure, and bubble-free samples. The differences between the two procedures are the growth temperature

and the method by which the system is flushed of undesirable gases, such as water vapor. The growing temperature was changed to give larger crystals, and the outgassing procedure was changed to reduce the bubble content in the crystal boules.

Undoped potassium zinc fluoride was grown from a stoichiometric mixture of Optran zone-refined crystal pieces of potassium fluoride and Optran zinc fluoride powder which were mixed and placed into a graphite crucible containing approximately  $1 \text{ mm}^3$  of anhydrous ammonium bifluoride. The graphite crucible, which was used in all cases except one and which had an inside diameter of 1.25 cm and a height of approximately 16 cm, was made from Ultra Carbon Corporation grade UT-9 graphite. The ammonium bifluoride decomposed at about 200 C, releasing hydrogen fluoride gas which flushed some of the adsorbed water out of the system. A screw cap containing a small hole to relieve the pressure inside the crucible was placed on the crucible, which in turn was placed into the ceramic tube. The ceramic tube was connected to the pumping system via the quick disconnect fitting. This procedure was performed as rapidly as possible in order to minimize the exposure of the potassium fluoride to the air, thereby reducing the amount of adsorbed moisture on this highly hygroscopic compound. If the humidity in the room was high, then the weighing of the potassium fluoride was done in a dry box. The system was then pumped very slowly so that the escaping

gases from the graphite crucible did not force any of the starting materials through the small hole in the cap. After a good fore pump vacuum was obtained, the diffusion pump was activated. When the pressure was between 15 and 30 microns, the furnace, which was in its lowest position, was turned on with a set point temperature of 300 C and with a current limit of approximately six amperes. The furnace heated the system to the set point of 300 C and was kept at this temperature with a diffusion pump vacuum for a minimum of eight hours. After this initial outgassing period, the set point was increased to a temperature of 750 C with a current limit of 12 amperes. After approximately five hours, the set point was increased to 1150 C and the current limit to 13 amperes. When this temperature was reached, the furnace was moved past the graphite crucible at its maximum rate of 1.5 centimeters per hour. This allowed the entire crucible to be outgassed as the highest temperature portion of the temperature gradient swept past the entire length of the graphite crucible. After the furnace had been allowed to travel its maximum distance, it was reset to its starting position. This was done in at least two steps so that there was not a large thermal shock which would crack the crucible. When equilibrium was again established after about three hours, the pumps were valved off and the system was flushed with argon gas. With a pressure of about 700 Torr of argon, equilibrium was again established. The system was then ready to start the growth procedure.

Therefore, the furnace was raised at a rate of 1.5 millimeters per hour. After the furnace had traveled its full length of 23 cm, it was shut down in three steps in order to avoid cracking of the crucibles: first the temperature was reduced to about 750 C with a current limit of about nine amperes; then it was reduced to 500 C with current limited to 6.5 amperes; then the current was turned off. When room temperature was reached, the system was again flushed with argon gas; and the pressure inside the system was brought to one atmosphere. The ceramic tube was then removed. The boule slid out of the inner crucible when it was tapped gently. Usually the bottom two-thirds of the material removed from the graphite crucible was a single crystal of potassium zinc fluoride, and the top one-third was polycrystalline potassium zinc fluoride.

This procedure was used to grow sample K3. The nickel-doped samples were also grown by this method except that 56 milligrams of nickel fluoride (anhydrous) from the Research Chemical Corporation were added to the zinc fluoride powder. It should be noted that it took at least ten days to grow one crystal using the procedure described above.

#### Crystal Boule Descriptions

Through the use of the growth procedure previously employed at Oklahoma State University, small crystal boules weighing approximately five grams were obtained. These crystals contained large bubbles throughout. During the

modifications, large boules were obtained, up to 20 grams for 32 grams of starting material, which contained fewer bubbles. Boule number 062672, from one of the early attempts, was very small and contained numerous small bubbles throughout; sample K1 was cut from this boule. Boule number 082572 was grown in a graphite crucible having approximately three times the volume,  $57 \text{ cm}^3$ , of the standard crucibles. The problems of crystal size were solved at this point, giving 44.9 grams of crystal for a 96 gram charge, but the crystal contained numerous bubbles; however, almost all the bubbles were located in the lower one-third of the crystal. Sample K2, which was very large and long, was cut from this boule. The region where the thermometers were placed on this sample was bubble free to the naked eye. Boule number 010473, from which sample K3 was cut, was grown by the procedure described in the preceding section. The boule's single crystal portion had a weight of approximately 20 grams with only a few bubbles in a region near the bottom of the crystal. After it was cut, the sample appeared to contain no bubbles. The two nickel-doped samples were cut from boule number 011873, which was grown by the same procedure as sample K3. A nickel doping of 0.1 percent was attempted. The resulting boule weighed approximately 15 grams.

#### Preparation of Samples

Although potassium zinc fluoride does not cleave



easily, cleaving was attempted on a corner of each boule until a cleavage plane was obtained. The blade of an IMANCO Macrotome diamond saw was aligned with this cleavage plane as a guide. The samples were cut into parallelepipeds of dimensions given in Table I.

The samples were then hand lapped using a #600 grit WETORDRY TRI-M-ITE PAPER (Waterproof Silicon Carbide) and methanol. This lapping produced a coarse surface which should give diffuse specular reflection off the crystal surface, thus producing the desired boundary scattering. After the thermal conductivities of sample KN1 were measured from 1.1 to 200 K, it was annealed in a vacuum at a temperature of 650 C for six hours and remeasured; there were no changes in its thermal conductivities.

#### Characterization

In thermal conductivity measurements, it is important to know as much as possible about the types and concentrations of all the impurities present in the crystal samples.

The impurity specifications given by the manufacturer, B D H Chemicals Ltd., for their Optran-grade zinc fluoride powder used in the starting material were 10 to 100 micrograms of cadmium and silicon, 1 to 10 micrograms of copper and iron, and less than 1 microgram of arsenic, beryllium, and magnesium for 1 gram of zinc fluoride. The concentration of these impurities in the single crystal, however, was expected to be much less, as much as one-tenth less,

TABLE I  
DIMENSIONS OF SAMPLES

Sample	Length (mm)	Width (mm)	Height (mm)
K1 KZnF <sub>3</sub> : undoped	12.5	3.27	2.64
K2 KZnF <sub>3</sub> : undoped	38.2	4.45	3.55
K3 KZnF <sub>3</sub> : undoped	16.8	2.84	2.64
KN1 KZnF <sub>3</sub> : Ni-doped	12.5	2.94	2.84
KN2 KZnF <sub>3</sub> : Ni-doped	20.3	4.04	3.60

than the values listed. Butler (82) states that electron paramagnetic resonance shows the impurities of manganese at ten micrograms per gram and of chromium and vanadium at concentrations of approximately one microgram per gram of zinc fluoride.

The potassium fluoride was also supplied by B D H Chemicals Ltd. It was zone-refined Optran-grade crystal pieces with a purity of 99.999 percent. Reagent-grade anhydrous nickel fluoride was supplied by the Research Chemical Corporation (ROC/RIC). Although it was a minimum of 98 percent pure, the impurities, primarily 0.10 percent cobalt and 0.01 percent iron, were of no consequence since only a very small quantity of nickel fluoride was used in the melt. An iron concentration of 100 to 150 parts per million was determined to be in the undoped and doped potassium zinc fluoride by the Oklahoma State University Soil Test Laboratory, which used atomic absorption spectroscopy.

Electron paramagnetic resonance measurements were made on one undoped sample and two nickel-doped samples. The undoped sample was cut from boule number 010473. The two nickel-doped samples were cut from boule number 011873, one from the end of the boule which was crystallized last and the other from the other end of the boule. The nickel-doped sample from the top of the boule was clear, and the electron paramagnetic resonance showed a peak for the nickel which was approximately three times stronger than

that of the undoped sample; and the signal for the sample cut from the center, which was yellow-green, was approximately six times stronger. All three samples showed strong electron paramagnetic resonance signals for iron.

Optical measurements on the undoped and doped samples showed a weak absorption in the nickel-doped samples at 415 nm with a width of 60 nm. There were no other peaks in the visible or ultraviolet spectrum. The infrared spectrum was scanned between  $800 \text{ cm}^{-1}$  and  $4000 \text{ cm}^{-1}$  with no peaks observed.

#### Experimental Determination of Thermal Conductivity

For a steady-state flow of heat through a solid having a temperature gradient  $\nabla T$ , the thermal conductivity,  $\lambda$ , is defined by the relation

$$Q = \lambda \nabla T \quad [39]$$

where  $Q$  is the energy transmitted across unit area per unit time. In the special case of a long, rod-shaped solid having a uniform cross-sectional area,  $A$ , with the heat flow along the long axis of the sample, Equation [39] becomes

$$\frac{P}{A} = \lambda \frac{\Delta T}{\Delta X} \quad [40]$$

where  $P$  is the power supplied to one end of the sample and  $\Delta X$  is the distance between which the change in temperature  $\Delta T$  is measured. To calculate the thermal conductivity from the experimental data where the input power is known, one experimentally measures the temperature difference  $\Delta T$  and

from the dimensions of the sample's cross-sectional area,  $A$ , and thermometer separation,  $L$ , determines the geometrical factor  $L/A$ ; Equation [40] is solved to give the thermal conductivity by

$$\lambda = \left( \frac{L}{A} \right) \frac{P}{\Delta T} \quad [41]$$

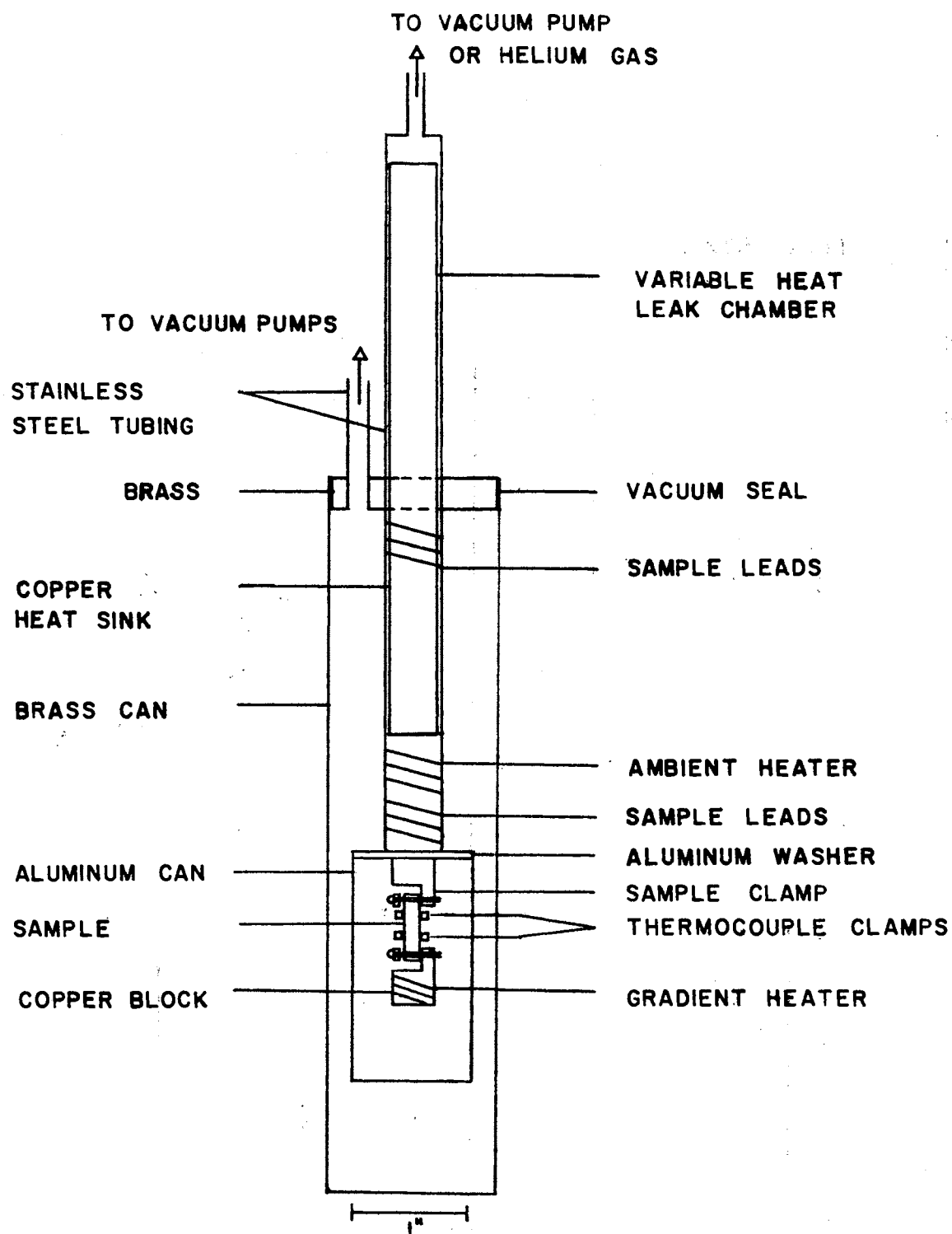
### Sample Holders

For the large temperature range in which the thermal conductivity measurements for these samples were taken, 0.42 to 200 K, three separate apparatuses had to be employed. Each apparatus took advantage of the techniques most suitable for the temperature range in which it was used, but each employed the standard steady-state heat flow technique. Their primary differences were the methods of obtaining and of measuring the temperatures.

#### Thermal Conductivity Between 3 and 200 K

The first apparatus was used for measuring the thermal conductivities of the undoped and doped potassium zinc fluoride in the temperature range 3 to 200 K. This apparatus is described in considerable detail by Whiteman (83) and Velasco (84); therefore, only a brief description will be given here.

Figure 3 shows a schematic of the sample holder. The sample was mounted at the end of a copper rod which was constructed so that the effective thermal contact with the



Source: 84

Figure 3. Thermal Conductivity Sample Holder for 3 to 200 K

cryogenic liquid bath, either liquid helium IV or liquid nitrogen, could be controlled by controlling the pressure of helium gas in the heat leak chamber. When helium gas was put into this chamber, the thermal contact with the cryogenic bath was good, giving the copper rod the same temperature as the bath. If the sample was heated and transmitted heat to the copper rod or if a current was passed through the 100 ohm ambient heater wrapped around the copper rod, the heat was quickly dissipated into the bath, approximately maintaining the bath temperature. If the thermal contact between the copper heat sink and the cryogenic bath was reduced by pumping some of the helium gas out of the heat leak chamber, then the heat dissipated to the copper heat sink was not removed efficiently and raised the temperature of the heat sink and sample. With a good vacuum in the heat leak chamber, the heat sink was effectively isolated from the cryogenic bath; therefore, temperatures much higher than the bath's could be reached. If the cryogenic liquid was helium IV at 4.2 K, temperatures as high as 50 K could be reached with less than 250 milliwatts of input power. If liquid nitrogen at 77 K was the cryogenic liquid, temperatures above 200 K could be obtained with approximately one watt of input power. At the higher temperatures, radiation heat loss became a large source of error when the sample temperature was greatly different from that of the outer wall of the sample holder. For reduction of this radiation loss, an aluminum heat

shield was placed around the sample, its clamps, and its gradient heater. This aluminum shield was in thermal contact with the copper heat sink rod and was therefore kept at approximately its temperature, greatly reducing the temperature difference between the sample and its surroundings. The entire assembly described above was enclosed in a brass can which was then submerged into the cryogenic fluid. When measurements were being taken, a vacuum of less than  $10^{-5}$  Torr was maintained inside the brass can, thus insuring proper temperature and heat loss control.

The sample was held in thermal contact with the heat sink by a copper clamp containing indium pads which flattened against the sample when the nylon screws were tightened. A phosphor bronze spring and the nylon screws compensated for the difference in the thermal expansion between the sample and the clamp. The two thermometer clamps were constructed in a similar manner (83, 85).

In all the samples except K2, the temperature gradient in the sample was established by a 120 ohm (at 4.2 K) heater clamped onto the end of the sample farthest from the heat sink. Sample K2 had a 94 ohm (at 4.2 K) heater wound around the end of it. Current was supplied to the heaters by #40 copper wires, and the voltage drop across the heaters was measured through #36 constantan wire.

The thermometers used in this apparatus were chromel versus gold-0.07 atomic percent iron. They were soldered to the clamps with indium solder so that the emf of T and



$\Delta T$  was read directly using a potentiometer. The potentiometer used to measure  $T$  was a Leeds and Northrup type K-3 Universal potentiometer in series with a Model 2770 Honeywell potentiometer with a Leeds and Northrup 9838 guarded nanovolt detector as a null indicator, thus allowing the emf to be resolved to the nearest 0.1 microvolt. The Honeywell potentiometer and nanovolt detector were used for measuring  $\Delta T$  with a 0.01 microvolt resolution. The gradient heater voltage and current were monitored on a Triplet D. C. millivolt digital panel meter, giving accuracy to three or four significant figures, depending on the magnitude of the current supplied to the heater. A stable current to the gradient heater was delivered by a twelve-volt storage battery. All of the leads leading into and out of the sample holder were thermally anchored to the copper heat sink with GE-7031 varnish.

#### Thermal Conductivity Between 1.2 and 4 K

The second sample holder measured the thermal conductivities between 1.2 and 4 K. A schematic of this sample holder is given in Figure 4. The basic difference between this apparatus and the previous one was that the heat leak chamber was replaced by a pot in which liquid helium IV could be pumped to reduce the temperature to as low as 1.2 K. Another major difference was that carbon resistance thermometers were used.

Since the size of this sample holder was about the

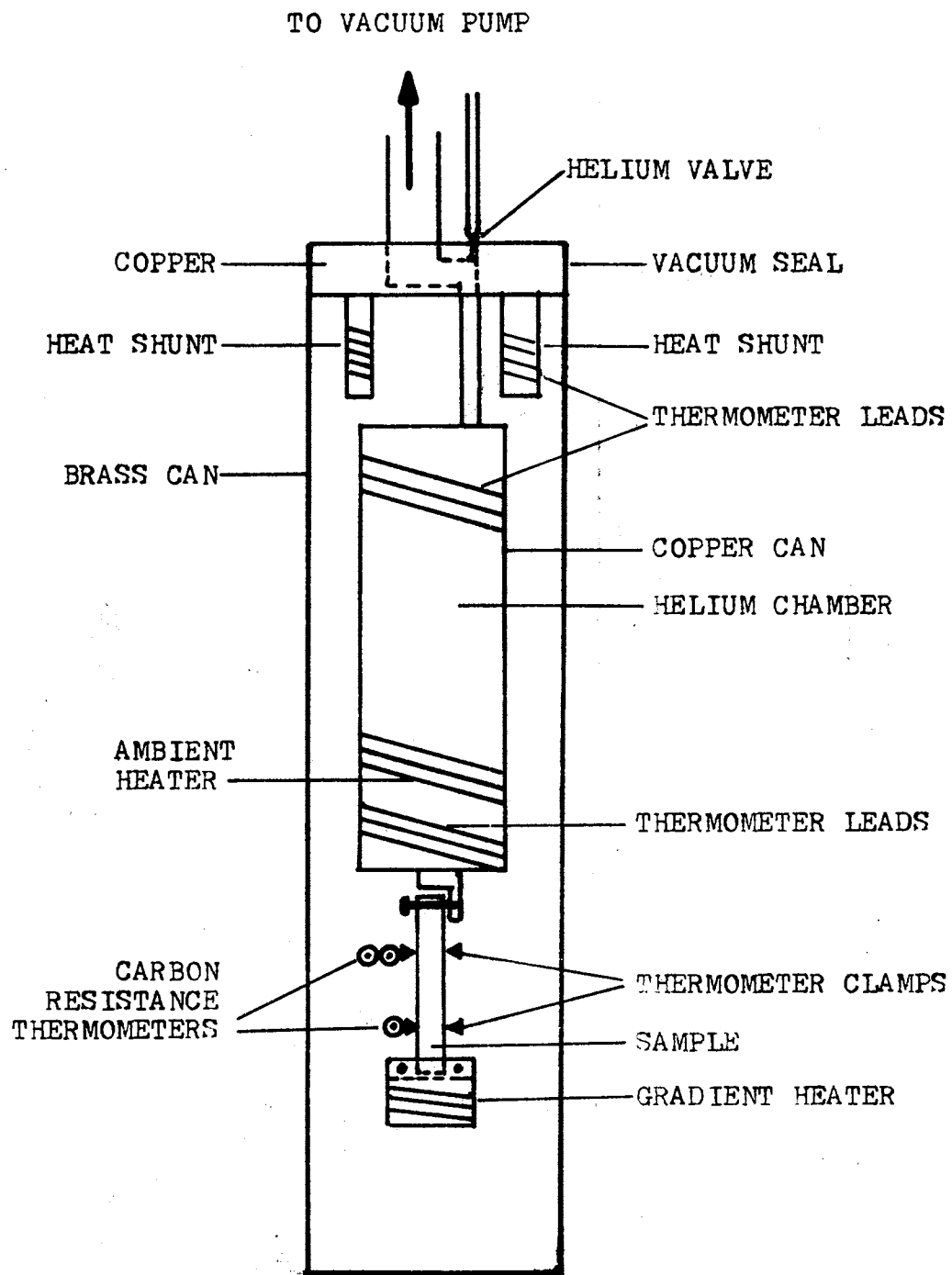


Figure 4. Thermal Conductivity Sample Holder for  
1.2 to 4 K

same as that of the one previously described, the same cryostat and pumping system for the sample chamber were used for both. The copper helium IV pot had a volume of approximately  $50 \text{ cm}^3$ ; and when the sample chamber had a vacuum of better than  $10^{-5}$  Torr, its only contact with the liquid helium bath was through a thin-walled stainless steel tube  $2\frac{1}{2}$  cm long. A small hole drilled through the vacuum seal leading into the stainless steel tube and a threaded brass rod with a point which could be screwed into this hole acted as a valve between the helium IV pot and the cryogenic bath. When the brass rod was screwed into the hole, this valve was closed; then the pot was effectively isolated from the bath. To reach the various temperatures at which a thermal conductivity measurement was desired, one pumped the pot through the stainless steel tube. By adjusting the pumping speed of the roughing pump by means of opening or closing a needle valve, one could obtain any temperature between 1.2 and 4 K.

The sample was mounted just as before. The indium-faced clamps were similar to those used before except that carbon resistors were mounted on them in place of the thermocouples as shown in Figure 5. The same gradient heaters were used, and a 100 ohm ambient heater was wound around the helium IV pot and used only for small adjustments in sample temperature. All the wires were thermally anchored to the helium IV pot and then to the helium IV bath.

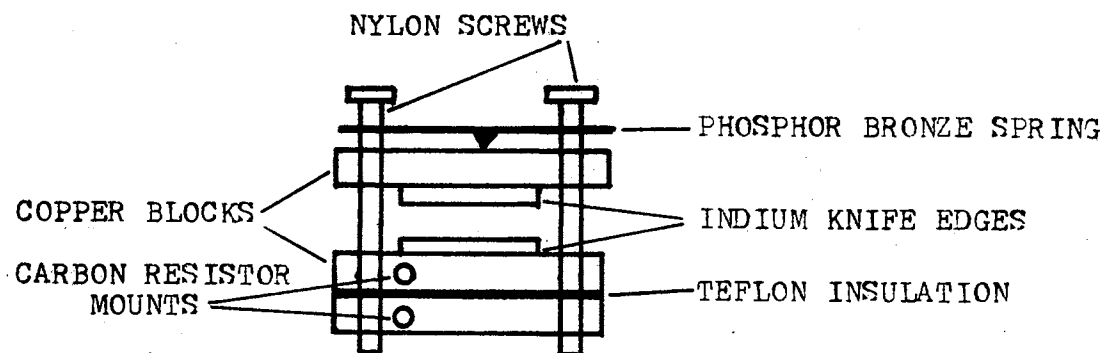


Figure 5. Sample Clamps for Carbon Resistance Thermometers

Measuring the resistance of resistor number one, the type of which is discussed in the section on thermometry, gave the temperature of the cold end of the sample; and measuring the difference between the resistances of resistors number two and number three gave the temperature difference,  $\Delta T$ , between the two clamps. These measurements were obtained by using two independent a.c. resistance bridge circuits as shown in Figures 6 and 7. In the circuit for measuring  $T$ , a three-terminal bridge was employed which eliminated the effect of lead resistance.

Thermal Conductivity Between 0.42  
and 1.5 K

A helium III pot system and resistance thermometry were used for measuring the thermal conductivities between 0.42 and 1.5 K. The same circuits as the ones shown in Figures 6 and 7 were used with Speer resistor thermometers. This elaborate system also had the capability of measuring the thermal conductivity of the sample in magnetic fields up to 70 KG. Figure 8 is a diagram of the helium III cryostat, and Figure 9 shows the sample chamber in greater detail.

The resistance thermometers were thermally mounted to the sample clamps through a #14 gauge copper wire approximately 25 cm long. This was required so that when a magnetic field was used, the carbon resistors were located outside the strongest part of the field, thus avoiding

TO LOCK-IN AMPLIFIER

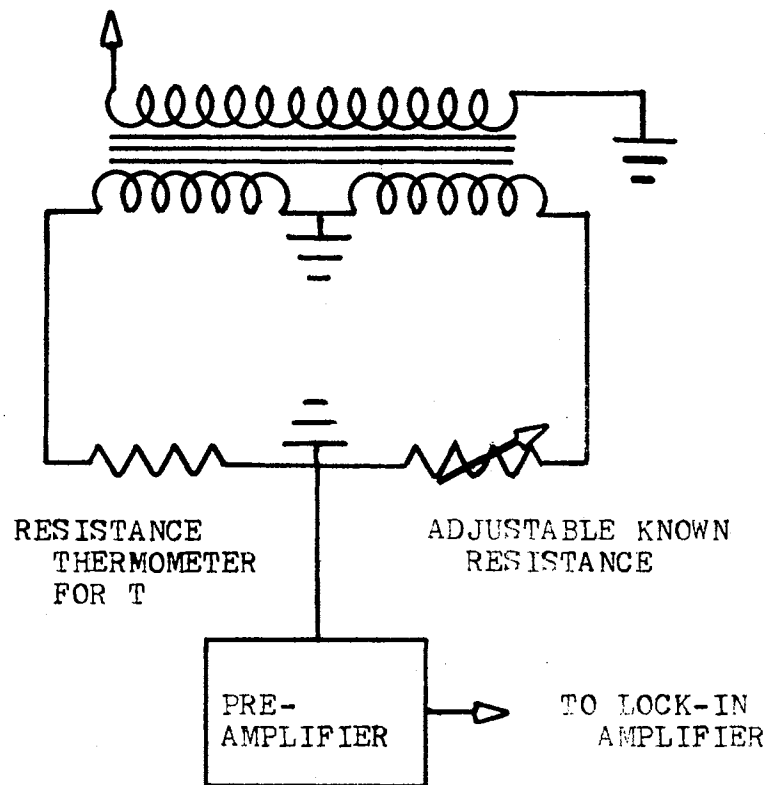


Figure 6. A. C. Bridge for Measurement of T in Thermal Conductivity Apparatus for 0.42 to 1.5 K

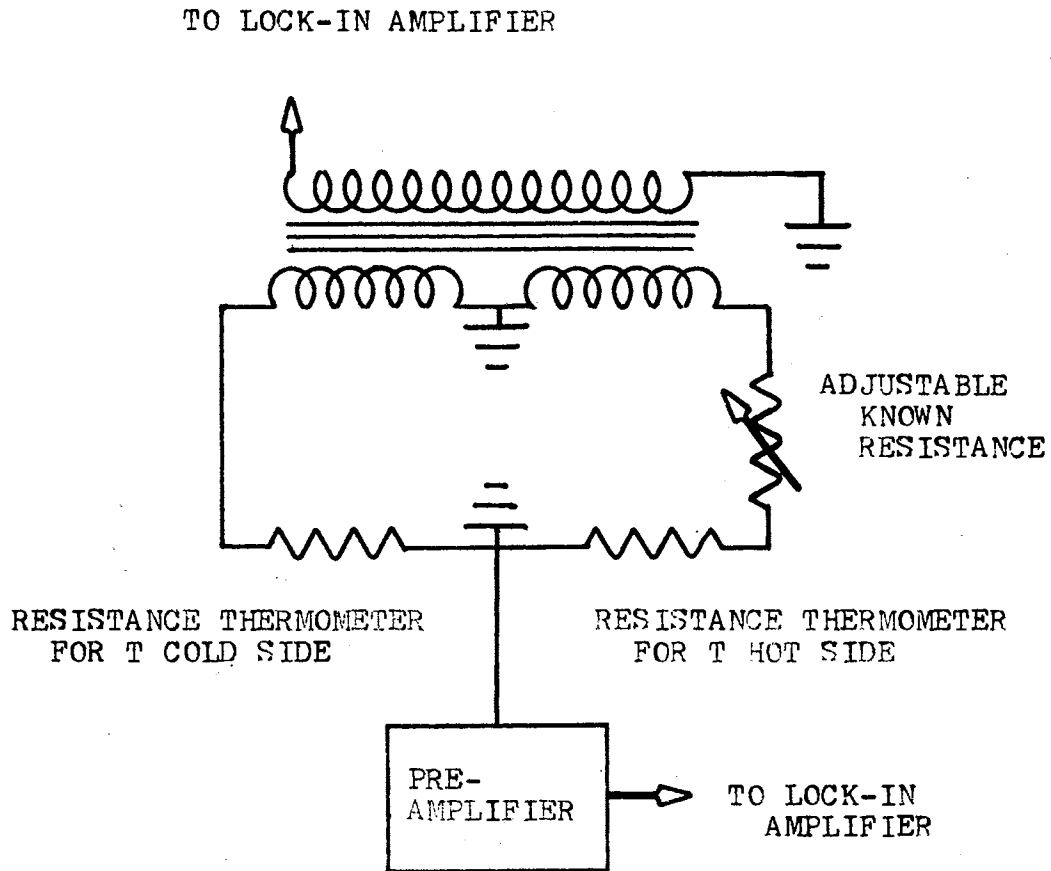
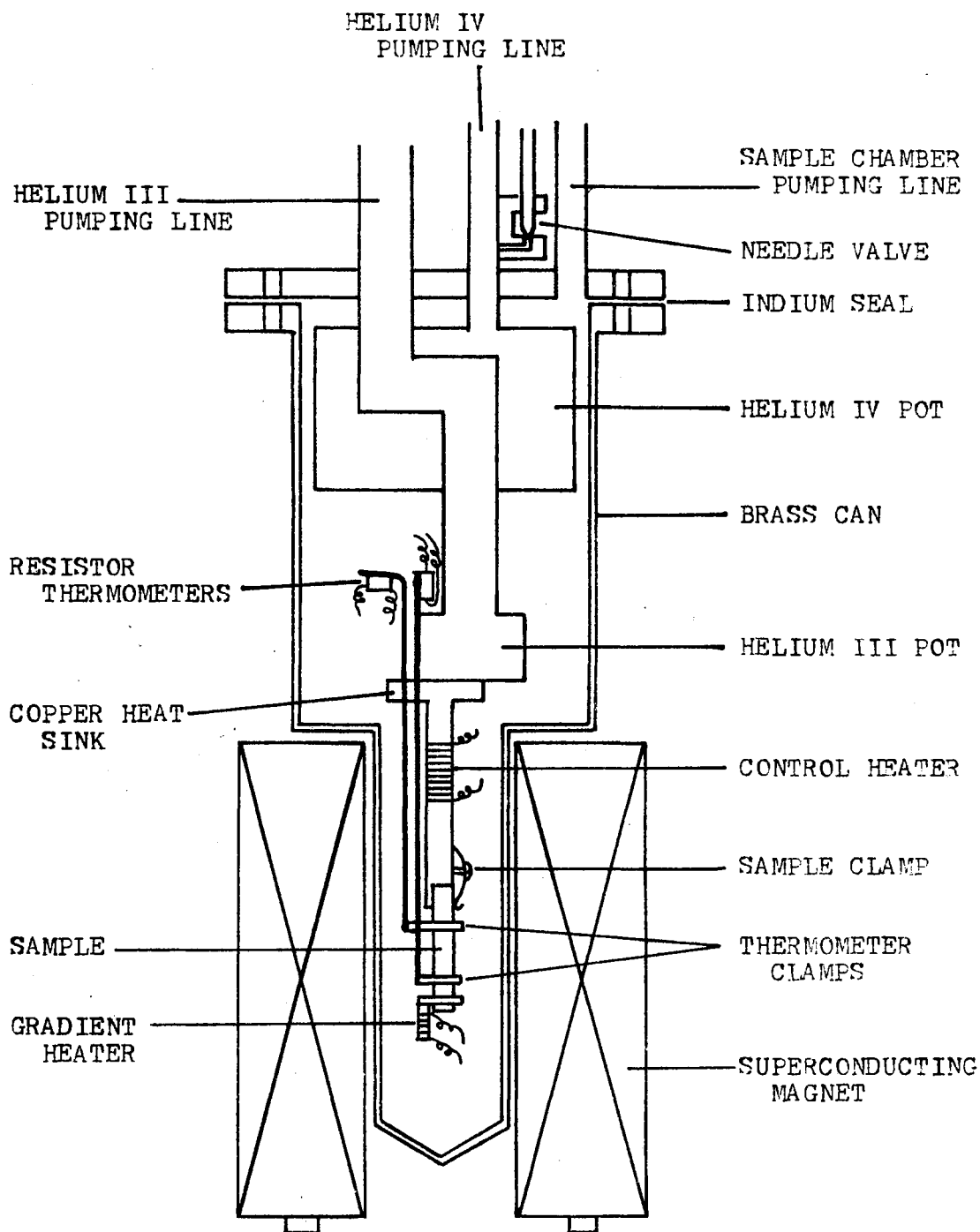


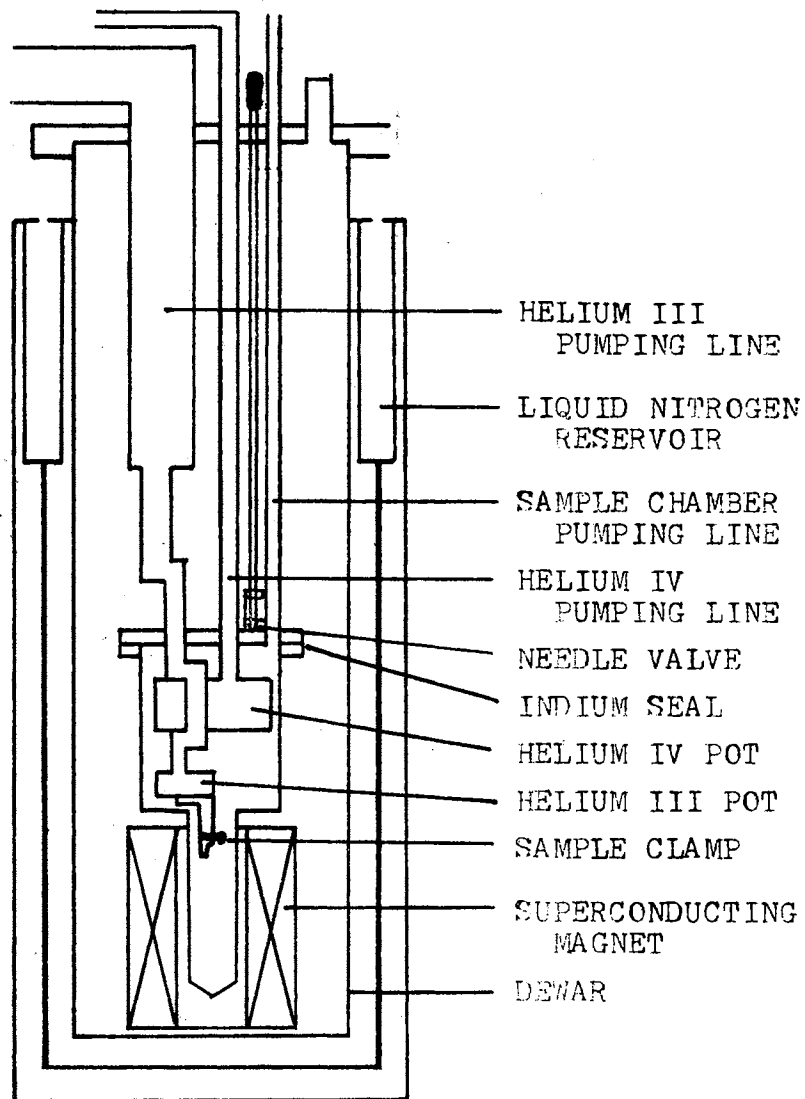
Figure 7. A. C. Bridge for Measurement of  $\Delta T$  in Thermal Conductivity Apparatus for 0.42 to 1.5 K



Source: 91

Figure 8. Sample Chamber of the Cryostat for Thermal Conductivity Apparatus for 0.42 to 1.5 K





Source: 91

Figure 9. Helium III Cryostat with Associated Equipment for Thermal Conductivity Apparatus for 0.42 to 1.5 K

calibration problems. The heater, which was the same one as was used in the other apparatus, was mounted on the end of the sample; and the other end was mounted to the copper heat sink. An ambient heater was wound on the heat sink allowing some control of the sample's temperature. The copper heat sink was in thermal contact with a helium III pot which had a thin-walled stainless-steel tube in thermal contact with a helium IV pot. Both these pots were contained in the sample chamber as shown in Figure 9. The helium III pot was filled with helium III gas through the stainless-steel tube running past the helium IV pot and then out of the chamber and cryostat. The helium IV pot was filled by opening a needle valve as shown in Figure 9 and allowing liquid helium IV to flow into the chamber from the cryogenic bath in which the chamber was submerged. When the vapor pressure in the helium IV pot was reduced by pumping to about 2.16 mm of mercury, giving the pot and heat sink a temperature of 1.4 K, the helium III gas began to condense in the stainless-steel tube and to run down into the helium III pot, when then reduced the temperature of the heat sink and sample. When as much helium III as possible had condensed in the pot, it was slowly pumped with a roughing pump and could reach temperatures as low as 0.5 K. For further temperature reduction, a diffusion pump was used. In all phases of pumping, the pumping speed was controlled by means of throttle valves.

## Thermometry

In the apparatus for measuring the thermal conductivities between 3 and 200 K, the temperature was determined using a chromel versus gold-0.07 atomic percent iron thermocouple. The gold-0.07 atomic percent iron was used as the negative element because of its high thermopower for the temperature range 3 to 30 K. (This thermocouple was Teflon-coated 5-mil diameter wire and was made from bar #2 and annealed by the manufacturer, Sigmund Cohn Corporation.) Chromel (Teflon-coated 5-mil diameter wire supplied by Omega Engineering Inc.) was used as the other element because of its high positive thermopower for the higher temperatures. Above the temperature range where the thermopower of the gold-0.07 atomic percent iron became small, that of chromel became appreciable, approximately 17 microvolts per degree in the liquid nitrogen temperature range, and increased the sensitivity (thermopower) smoothly to about 22 microvolts per degree at room temperature. Combined, these two elements gave excellent sensitivity for the entire temperature range of 3 to 300 K. The emf versus temperature remained within five percent of being linear through the temperature range, which was important because the calibration points were spread out, giving large temperature intervals between points, particularly above 20 K. Since there was this near-linear response, extrapolations of the fitted curve to lower and higher temperatures and interpolations between calibration points could be made

safely without introducing large errors.

Since the composition and production history of each spool of wire used in the thermocouple might vary from one spool to the next, the standard thermocouple tables had to be modified to fit the characteristics of the present thermocouple used. The chromel versus gold-0.07 atomic percent iron thermocouple was calibrated using helium IV vapor pressure techniques. Temperatures below 4.2 K were obtained by pumping the cryogenic helium IV bath, and the temperature of the bath was determined by measuring the helium IV vapor pressure using a mercury monometer and the 1958 helium IV vapor pressure scale. For temperatures above 4.2 K, a platinum resistance thermometer was used for determining the thermocouple's temperature. The emf obtained for each calibration point was subtracted from the value obtained by the National Bureau of Standards (86) as listed in the calibration table for chromel versus gold-0.07 atomic percent iron thermocouples. This difference was plotted, giving a difference curve of emf's versus temperature. The maximum difference between the Oklahoma State University thermocouple and the National Bureau of Standards thermocouple was 23 microvolts at liquid helium IV temperatures. This difference reduced to 6 microvolts at about 30 K and remained within  $\pm 6$  microvolts to the ice point. This difference curve was divided into three intervals: 3 to 45 K, 45 to 120 K, and 120 K to room temperature; and each interval was fitted with a polynomial

of third degree. Through the use of these fitted polynomials as a correction to the values in the National Bureau of Standards table, a table was generated which gave the emf of the Oklahoma State University thermocouple referenced to ice for the temperatures between 1 and 300 K.

In the apparatus for measuring the thermal conductivities from 1.2 to 4 K, a system of differential carbon resistance thermometers was used. The thermometers were commercial Allen-Bradley Company resistors with a room temperature resistance of approximately 30 ohms. In the temperature range 1.2 to 4 K, these resistors had extremely high sensitivities, ranging from 27.6 kilo-ohms per degree at 1.20 K to 151 ohms per degree at 4.00 K. One of the major advantages of these resistors was that the resistance versus temperature gave a smooth curve. A log-log plot of resistance versus temperature gave almost a straight line between 1.2 and 2.5 K with a slow change from linearity up to 4 K. Therefore, the calibration points were fitted with a function of the form

$$\log T = \sum_{i=0}^N C_i (\log R)^i \quad [42]$$

where R is the resistance of the thermometer at temperature T, and  $C_i$  is the coefficient of the  $i^{\text{th}}$  term for the N term interpolation formula obtained by a least-squares fit of the calibration data. It was determined that  $i = 3$  gave excellent fits for each set of calibration points.

Calibration data were obtained by means of a mercury

or oil monometer, whichever was appropriate for that temperature, each time a power zero background reading was taken. The response of these thermometers to a small change in vapor pressure was extremely rapid.

The third apparatus, which was used for thermal conductivity measurements between 0.42 and 1.5 K, used Speer Company resistors of approximately 600 ohms at room temperature. The resistance changed smoothly from 1.85 kilo-ohms at 1.37 K to 7 kilo-ohms at 0.3 K. The sensitivity at 1.37 K was approximately 893 ohms/K. The functional variation of Speer resistors was quite different from that of the Allen-Bradley resistors in such a way that they were well suited for the lower temperatures. A polynomial of the form

$$T^{-1} = \sum_{i=0}^N C_i x^i \quad [43]$$

where  $x = (R - R_L)^{\frac{1}{2}}$  was used for the calibration data. The temperature of the sample is  $T$ ,  $C_i$  is the coefficient of the  $i^{\text{th}}$  term,  $R_L$  is the lead resistance, and  $R$  is the thermometer resistance. A six parameter form,  $N = 6$ , was found to give the desired accuracy. The calibration data were obtained by using helium III vapor pressure and susceptibility techniques. Forty calibration points were used for the range 0.3 to 1.5 K.

## Errors

### Measurement Errors

The errors in the thermal conductivity calculations made using Equation [41] depended on the absolute and relative precision in the measurements of the sample cross section, thermometer separation, input power, sample temperature, and gradient temperature.

The dimensions used to calculate the cross-sectional area,  $A$ , were measured with a micrometer to the nearest 0.01 mm. Since none of the samples was a perfect parallelepiped, each end was measured with the average values used in the calculation. Therefore, the percent variation for the cross-sectional area was a maximum of 0.8 percent for the smallest sample, K3; the other samples had a smaller percentage of uncertainty.

The measurement of the thermometer spacing was the most uncertain measurement taken. The clamp separation,  $L$ , was determined by placing a spacer, whose thickness was measured with a micrometer, between the two thermometer clamps. The clamps were pressed against the spacer with a slight pressure and tightened. The spacer was pulled straight out so that movement of the clamps to one side could be avoided. Previously the clamps' thicknesses were measured with a micrometer. To find the clamp separation, one added half of each clamp's thickness and the spacer's thickness. If the spacer was firmly against each clamp

and they were not moved when the spacer was removed and if the assumption was made that the temperature measured was the temperature at the center of the clamp, then the percent variations in these measurements would be 0.5 percent for the smallest clamp separation used (sample K1) and 0.2 percent for the largest (sample K2). The error could be expected to be much greater for any particular measurement. However, the thermal conductivity curve of a sample was reproducible to within two or three percent from one mounting to another (87). Except for sample K2, the above measurements of the cross-sectional areas and the clamp separations were made only once for each sample during a particular data run. Therefore, the uncertainties in these measurements remained constant and did not affect the shape of the thermal conductivity curve, but it may have been shifted from its true value by as much as ten percent.

The power input to the hot end of the sample was determined by measuring the current through the gradient heater. This current was read to four figures with an uncertainty of  $\pm 3$  in the last digit. When the current was less than 2 mA, it was determined by measuring the voltage drop across a 100 ohm standard resistor; and the voltage was read directly from the digital millivoltmeter with the same uncertainty in the fourth digit. The input power was calculated using  $P = IV$ . If the gradient current was larger than 2 mA, then the current was determined by measuring the voltage drop across a 10 ohm standard



resistor. The resistance of the heater at this temperature was determined by passing a 1 mA current through the heater and measuring the corresponding voltage. All the measurements had an uncertainty of approximately  $\pm 3$  in the fourth digit. The input power was then  $P = I^2R$ . The gradient current remained constant during each measurement, eliminating errors as a result of drift. The maximum error resulting from the determination of the input power would therefore be 0.9 percent. The relative uncertainty between data points, however, should have been much smaller since the meter's error would be in the same direction and should have approximately the same magnitude for each determination.

The above uncertainties in the thermal conductivity measurements were common to the two apparatuses for 1.2 to 4 K and for 3 to 200 K and, with some minor modifications, for the very low temperature apparatus; however, the measurement of the errors for the sample and gradient temperature must be considered individually for each type of thermometer used. The total uncertainties in the standard calibration table for the chromel versus gold-0.07 atomic percent iron thermocouple from which the table for this study was derived were as follows: 9.8 mK for the temperature range 4 to 20 K, 11.3 mK for 20 to 75 K, and 31.9 mK for 75 to 280 K (88). According to Sparks (88), these estimates include the inaccuracies in the measurements and in the curve fitting. The modification of the table

according to the calibration procedure discussed in the section on thermometry probably introduced larger uncertainties in the table. For the calibration data below 4.2 K, the helium IV vapor pressure was measured, giving data accurate to within 0.2 percent of the actual vapor pressure. Additional uncertainties were introduced in generating the present table, as described in the section on thermometry.

Using the K-3 potentiometer, one could measure the voltage to  $\pm 0.5$  microvolt, which corresponded to a maximum temperature uncertainty of 40 mK at 4.2 K to 28 mK at 77 K. The relative uncertainty between data points and data runs, however, was considerably less than the total maximum errors given above. The reproducibility of the thermocouples was better than 0.02 percent on successive cool-downs (89).

Using the K-3 potentiometer in series with the Honeywell potentiometer allowed a resolution of 0.1 microvolt. This corresponded to an uncertainty of 8 mK at 4.2 K and 6 mK at 77 K. The measurements were taken when the sample temperature was in an equilibrium state; a drift of no more than  $\pm 0.1$  microvolt was allowed at 4.2 K and  $\pm 0.2$  microvolt at 77 K. The corresponding temperature uncertainty was 8 mK at 4.2 K and 12 mK at 77 K.

The errors in the  $\Delta T$  measurements were a great deal smaller than those above because a differential thermocouple was used which allowed relative measurements for the

change in temperature along the sample to be resolved to  $\pm 0.01$  microvolt or 0.8 mK at 4.2 K and 0.6 mK at 77 K. There was very little change in the thermopower of this thermocouple compared to that of Sparks (86) for any particular temperature, thus giving an almost identical response for the sensitivity of the two thermocouples, 0.06 percent at 4 K and 0.5 percent at 77 K. Table II gives a summary of the uncertainties described above.

The major uncertainties arising in the two resistance thermometry systems were the resolution of the resistance, drift during measurement, and accuracy in the calibration.

For the system employing the Allen-Bradley Company carbon resistors, the resolution of the resistance for measuring the sample's temperature and the amount of drift during the data taking are shown in Table III for three representative temperatures.

The resistance thermometer which measured the temperature of the cold end of the sample was calibrated during each run. Through the measurement of the helium IV vapor pressure with a mercury or oil monometer, whichever was appropriate for that temperature, a calibration point was obtained each time a "power zero" correction point was taken. For sample K2, 17 calibration points were taken; and for sample KN2, 14 were taken. A least-squares fit of these points, using a four parameter function of the form given in Equation [42], resulted in an average root-mean-square-deviation of 3.1 mK for K2 and 3.2 mK for KN2 be-

TABLE II  
 UNCERTAINTIES IN THE THERMOCOUPLES  
 (CHROMEL VERSUS GOLD-0.07%  
 IRON THERMOCOUPLES)

[All uncertainties are given in milli-Kelvins.]

	4.2 K	10 K	77 K	200 K
Sensitivities of Gold-0.07% Iron Thermocouples (in $\mu\text{V}/\text{K}$ )	12.6	16.0	17.8	21.3
<u>Uncertainties in T</u>				
Calibration (NBS)	9.8	9.8	11.3	31.9
Limits of K-3	40	31	28	23
Drift	8	8	11	11
Change in Calibration	0.8	2	15	40
Resolution of K-3 in Series with Honeywell	8	6	6	5
<u>Uncertainties in <math>\Delta T</math></u>				
Calibration Table	8	8	9	9
Limits on Honeywell	2	1	1	1
Resolution of Honeywell	0.8	0.6	0.6	0.5

TABLE III  
 SENSITIVITY AND RESOLUTION OF ALLEN-BRADLEY  
 CARBON RESISTANCE THERMOMETERS

[All entries in the table are in ohms, and quantities in parentheses are in micro-Kelvins ( $\mu\text{K}$ ).]

	1.2 K	2 K	3.5 K
Sensitivity	27.6 k $\Omega$ /K (36.2 $\mu\text{K}/\Omega$ )	2.44 k $\Omega$ /K (410 $\mu\text{K}/\Omega$ )	244 $\Omega$ /K (4.10 mK/ $\Omega$ )
Resolution of T	$\pm 1$ (40)	$\pm 0.5$ (200)	$\pm 0.1$ (400)
Resolution of $\Delta T$	$\pm 0.1$ (4)	$\pm 0.01$ (4)	$\pm 0.01$ (40)
Maximum Drift of T	$\pm 3$ (100)	$\pm 1.5$ (600)	$\pm 1$ (4000)
Maximum Drift of $\Delta T$	$\pm 0.15$ (5)	$\pm 0.05$ (20)	$\pm 0.01$ (40)

tween the calculated points and the vapor pressure points. A smaller deviation could be obtained through the use of higher order functions, but they were not used so that the possibility of oscillations between calibration points, which would result in erroneous values of the temperatures and the sensitivity, could be avoided. The sensitivity was determined by means of the fit constants determined in the least-squares fit. Representative values are given in Table III.

The mercury monometer was accurate to  $\pm 0.5$  mm of mercury and the oil monometer to  $\pm 0.04$  mm of mercury. Since the precision desired was not greater than 10 mK, the corrections required for extreme precision (90) were not made.

The very low temperature apparatus employed Speer Company resistors. The sensitivity and resolution of these resistors and the probable drift in the temperature during the measurement are shown in Table IV. The calibration data were obtained with helium III vapor pressure methods, and the resulting least-squares curve fit gave an uncertainty of approximately 4 mK.

A detailed error analysis and calibration procedure for an almost identical system are given by Hetzler (91).

#### Heat Loss Errors

Direct use of Equation [41] assumes that all the power that was calculated converted to heat that flowed uniformly

TABLE IV  
 SENSITIVITY AND RESOLUTION OF SPEER  
 CARBON RESISTANCE THERMOMETERS

	.33 K	1.2 K
dR/dT	21 k $\Omega$ /K ( $0.57 \times 10^{-4}$ K/ $\Omega$ )	1.2 k $\Omega$ /K (0.85 mK/ $\Omega$ )
Resolution in T (1 $\Omega$ )	0.06 mK	0.9 mK
Resolution in $\Delta T$ (0.1 $\Omega$ )	0.6 K	0.09 mK
Drift	0.2 mK	0.4 mK

through the sample. However, there were three major mechanisms by which the heat could be dissipated other than by flowing through the sample to the cold heat sink, resulting in erroneous values of  $\Delta T$  for the calculated power. These mechanisms were convection, conduction, and radiation.

Since the sample was in a vacuum of better than  $10^{-5}$  Torr, convection and conduction of the heat directly from the sample to the wall of the sample holder could be ruled out as dissipating heat. Conduction through the wire leads going into the sample chamber, however, must be considered. The total heat loss owing to conduction through  $i$  wire leads is

$$Q_{\text{Lead}} = \sum_i \lambda_i \frac{a_i}{l_i} \Delta T_i \quad [44]$$

where the summation is over all the leads,  $\lambda_i$  is the thermal conductivity of the  $i^{\text{th}}$  lead,  $l_i$  and  $a_i$  are its length and cross-sectional area respectively, and  $\Delta T_i$  is the temperature difference between its connection in the sample chamber and the heat sink. There were seven wires going into the sample holder: two copper and two constantan wires for the heater; two chromel wires, one for each thermocouple; and one gold-0.07 atomic percent iron thermocouple wire. Inside the sample chamber there was a 15-cm length of gold-iron wire, used for the differential thermocouple, connected between the sample clamps. Table V shows heat loss by each of these leads for various temperatures. The table shows that the power lost through the chromel wire was very



TABLE V  
HEAT LOSS THROUGH LEAD WIRES

Wire	2 K	10 K	200 K
Gold + 0.07% Iron	4 $\mu$ w	64 $\mu$ w	3 mw
Chromel	70 nw	2 $\mu$ w	0.3 mw
Copper	124 $\mu$ w	0.3 mw	3 mw

small, a factor which minimized the effects of heat loss through the leads; this was another of the reasons that chromel was chosen as the second thermoelement.

The thermal resistance of the 15-cm differential thermocouple wire at 10 K was approximately  $3 \times 10^6$  K·cm/W. Also, at this temperature the thermal resistance of sample K2 was 11 K·cm/W. Comparing these two values, one can see that because of the much higher thermal resistance of the differential thermocouple wire, practically all the heat flowed through the sample with no heat loss through the wire.

The radiation heat loss,  $Q_{\text{radiation}}$ , is approximated by

$$Q_{\text{radiation}} = 4 a' \sigma \epsilon T^3 \Delta T \quad [45]$$

where  $a'$  is the surface area of the sample,  $\sigma$  is the Stefan-Boltzmann constant,  $\epsilon$  is the emissivity of the sample,  $T$  is its temperature, and  $\Delta T$  is the difference between the sample's temperature and the chamber wall's temperature. At low temperatures the radiation heat loss was negligible, but at room temperature it could become quite significant. Because of this, data were only taken up to 200 K although the apparatus was designed for measuring thermal conductivities up to 300 K. To allow data to be taken at 200 K, one must surround the sample chamber with an aluminum can as discussed in the section describing the apparatus. Without this aluminum can, Equation [2] calculates a possible heat loss of approximately 80 mW at

200 K, which is larger than the input power. However, with the aluminum can, heat shield, which attained a temperature close to that of the heat sink, a heat loss of less than 9 mW could be expected for a temperature difference between the two of 13 K. Assuming that a maximum temperature difference between the aluminum can and the sample is one-tenth of the temperature difference between the heat sink and the cryogenic fluid and taking  $\epsilon$  as its maximum possible value, which is 1, Table VI gives comparative values of the radiation heat losses for the largest sample, K2, for three representative temperatures. The smallest sample, K1, would have heat losses of approximately 60 percent less than the values given in Table VI.

In the two very low temperature apparatuses, a possible source of error was self-heating as a result of the measuring current's passing through the resistors. A calculation of the power dissipated by this current was approximately 9 nanowatts at the  $\lambda$  point (2.16 K) and 0.1 nanowatt at 3.5 K. This power was insignificant when compared to the input power.

TABLE VI  
ESTIMATED RADIATION HEAT LOSSES

Temperature	Heat Loss
200 K	80 mw
100 K	2 mw
30 K	60 $\mu$ w

## CHAPTER IV

### RESULTS AND DISCUSSION

#### Results

The thermal conductivities of three undoped samples and two nickel-doped samples of potassium zinc fluoride single crystals were measured from 3 to 200 K. On one of the undoped samples, the measurements were extended to 1.2 K; and on one of the nickel-doped samples, the measurements were extended to 0.42 K. The data between 2.5 and 200 K for the undoped samples are presented in Figure 10. The shapes of the curves were characteristic for single-crystal insulating materials. For temperatures above 60 K, the thermal conductivities for all three samples were the same, having the characteristic slope of  $T^{-1}$  resulting from the dominance of three phonon-phonon interactions. In the peak region between 5 and 60 K, the thermal conductivities of K2 had a higher peak, approximately 37 percent different, probably as a result of differences in point defect scattering. Below 4 K the thermal conductivity curves of the three samples had a slope of approximately  $T^3$ . At much lower temperatures it appeared that the slope became larger than  $T^3$  as shown in Figure 11, which gives the very low temperature thermal conductivity of one

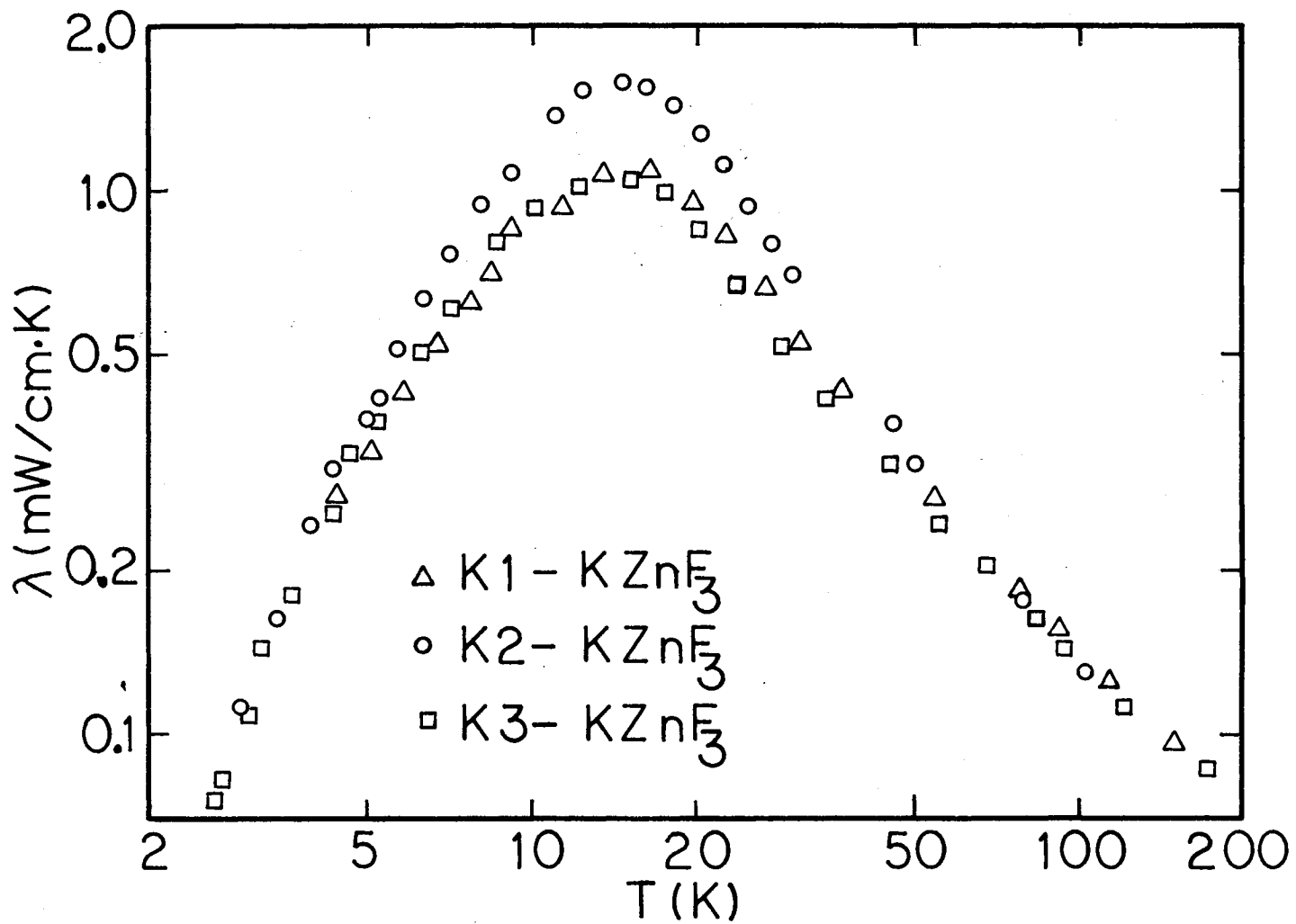


Figure 10. Thermal Conductivity of Undoped Potassium Zinc Fluoride

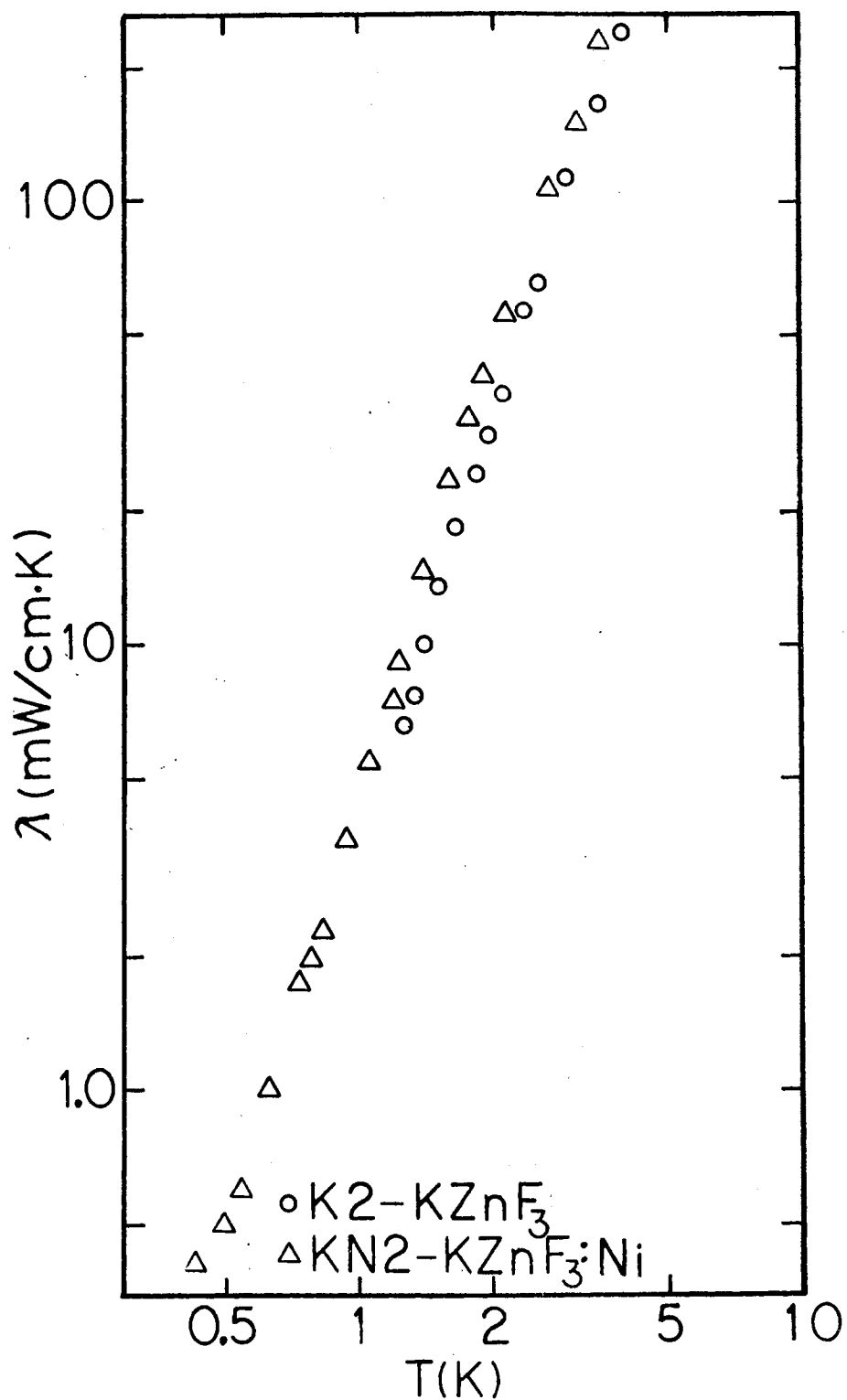


Figure 11. Low Temperature Thermal Conductivity Data of Undoped and Nickel-Doped Potassium Zinc Fluoride

undoped (K2) and one nickel-doped (KN2) sample. Figure 12 gives the thermal conductivity data for the nickel-doped samples for the same temperature range as in Figure 10. The curve of K2 is also given for comparison. The data points indicated on these curves represent one-third to one-half of the data taken for each sample. A tabulation of all the data points taken is presented in Appendixes B through F. Figure 13 shows the currently available thermal conductivity data for potassium zinc fluoride and other related perovskites. Suemune and Ikawa (92) measured the thermal conductivities of a number of the potassium divalent metal fluorides, but of most interest were the data on undoped potassium zinc fluoride; Velasco (84) measured undoped potassium manganese fluoride; and Harley and Rosenberg (93) measured undoped and nickel-doped potassium magnesium fluoride.

### Discussion

The thermal conductivities above the maximum were the same for all the samples measured. In this region, the phonon-phonon interactions were the dominant scattering mechanisms. Using the Roufosse and Klemens relation,

$$\lambda = \frac{3^{1/3} k^3}{2^{1/6} \pi^{4/3} \gamma^2 h^3} M a \theta^2 \frac{\theta}{T} \quad [38-a]$$

a value of 0.64 was obtained for the Grüneisen anharmonicity parameter using the measured thermal conductivity of 75 mW/cm·K at 200 K. A Debye temperature,  $\theta$ , of 274 K



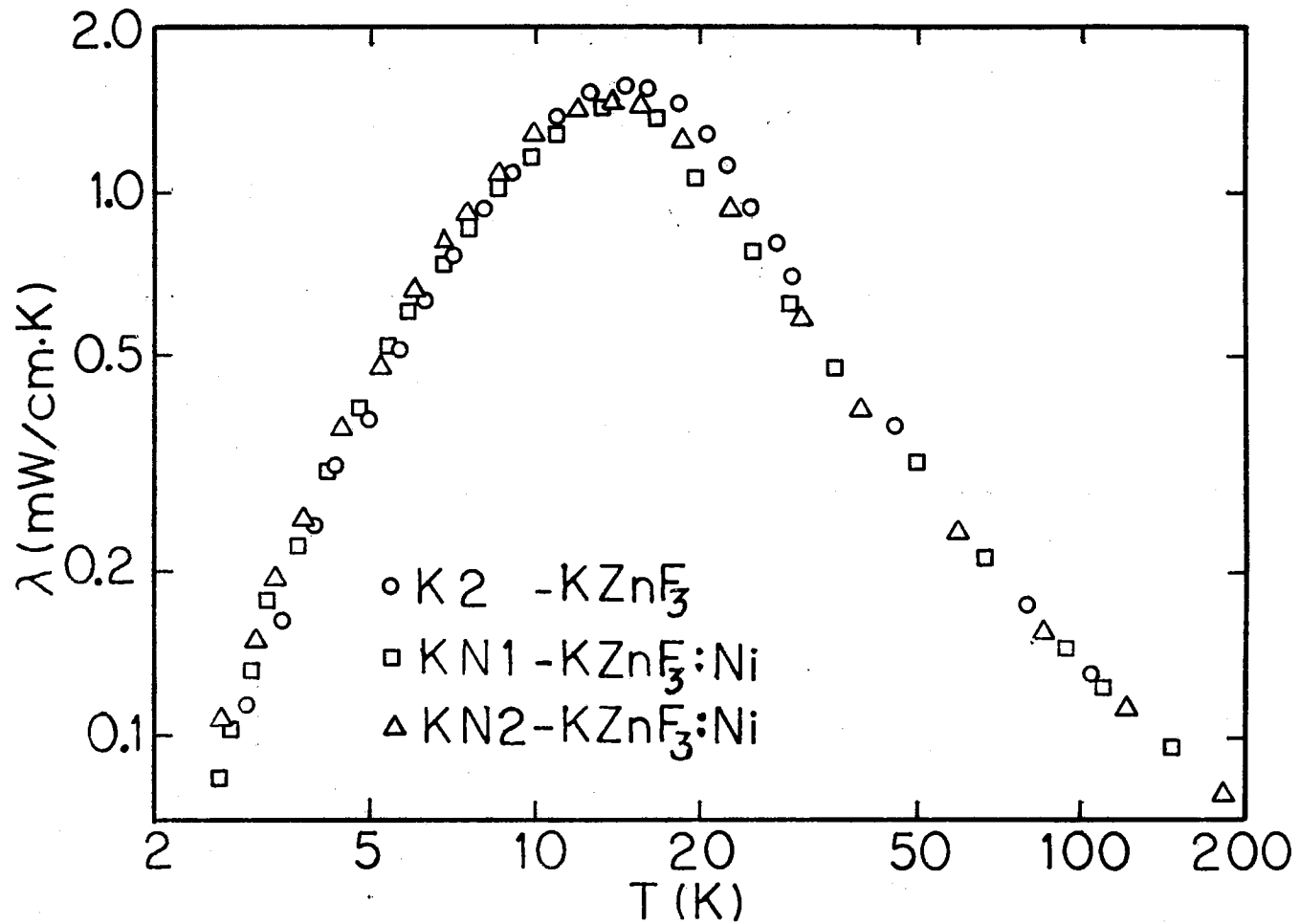


Figure 12. Thermal Conductivity of Nickel-Doped Potassium Zinc Fluoride

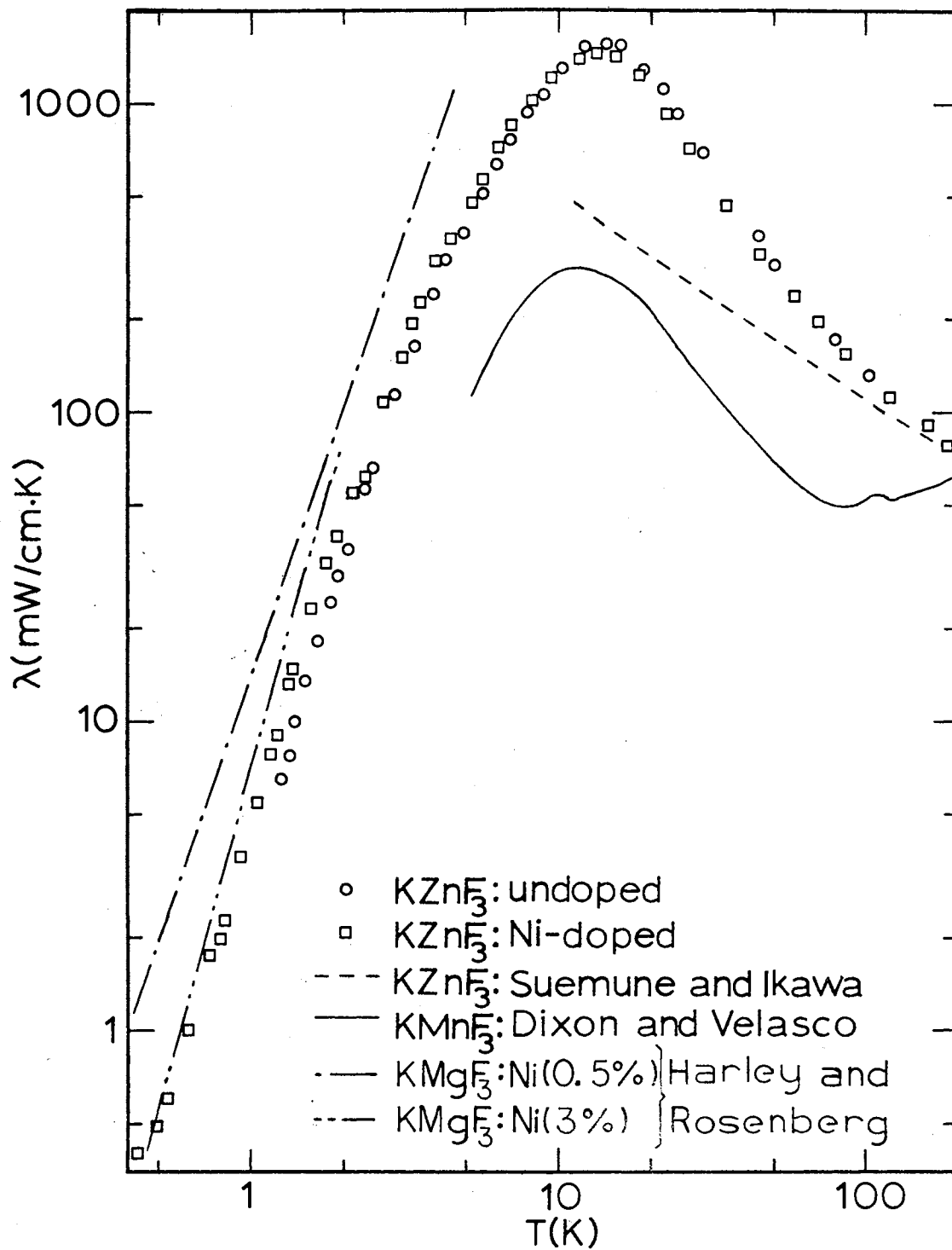


Figure 13. Thermal Conductivity of Related Perovskites

was calculated from the equation

$$\theta = \frac{\hbar}{k} \frac{v}{V} (6\pi^2)^{1/3} \quad [38-b]$$

The average sound velocity was calculated to be  $3.74 \times 10^5$  cm/sec using the relation

$$\frac{1}{v} = \frac{1}{3} \left( \frac{1}{v_\ell} + \frac{2}{v_t} \right) \quad [38-c]$$

where the transverse and longitudinal sound velocities were measured by Gesland et al. (24) as  $v_t = 3.19 \times 10^5$  cm/sec and  $v_\ell = 5.72 \times 10^5$  cm/sec. Although there are no published values of the Grüneisen parameter for potassium zinc fluoride to compare this to, it is a reasonable value for ionic insulating crystals. For example, in zinc oxide, which also has a cubic structure, Wolf and Martin (87) determined the Grüneisen parameter as being between 0.5 and 0.6 using the same procedure as in the present study.

Suemune and Ikawa (92) measured the thermal conductivities of a small crystal (1.5 mm x 1.5 mm x 10.0 mm) of undoped potassium zinc fluoride between the temperatures 12 to 300 K. Their results are given in Figure 11, which shows a temperature dependence above the peak region of  $T^{-0.64}$ . This temperature dependence is different from the result obtained in this study of  $T^{-1}$ , which is the expected dependence for phonon-phonon scattering in pure material. Suemune and Ikawa believed that their lower temperature dependence was due to impurity scattering of phonons, meaning that their samples contained a great deal more impurities than did the ones in this study.

The nickel-doped samples, KN1 and KN2, were both cut from the same boule but along different crystal planes. Since potassium zinc fluoride has a cubic structure, it would be expected that the thermal conductivity is not dependent on its orientation, which is shown to be the case in Figure 12. Figure 12 also shows that the thermal conductivities of the undoped sample K2 were the same as those of the nickel-doped samples for the temperatures between 5 and 200 K, indicating that the dilute nickel doping of less than 0.1 percent had no measurable effect on the thermal conductivities of potassium zinc fluoride for a zero applied magnetic field in this temperature range. The peak regions of the undoped samples K1 and K3 were lower than those of the undoped sample K2 and the two nickel-doped samples. This was due to an increase in point defect scattering in these two samples.

As stated in Chapter II, the common practice is to present thermal conductivity data of single crystal materials in terms of the Debye-Callaway model given by

$$\lambda = \frac{k}{2\pi^2 v} \left( \frac{kT}{\hbar} \right)^3 \int_0^{\frac{\theta}{T}} \tau_c \frac{x^4 e^x}{(e^x - 1)^2} dx \quad [46]$$

where  $x = \frac{\hbar\omega}{kT}$ . This integral employs a combined relaxation time, as given in Equation [37], obtained by reciprocal addition of the individual relaxation times.

$$\tau_{\text{Combined}}^{-1} = \tau_{\text{Boundary}}^{-1} + \tau_{\text{Isotope}}^{-1} + \tau_{\text{Phonon-Phonon}}^{-1} + \sum_{\text{All Others}} \tau^{-1} \quad [37]$$

For the large temperature range which this study's thermal conductivity data covered, the minimum number of possible relaxation times which could be used for a reasonable fit was three: boundary, isotope, and phonon-phonon. Since there was no  $T^2$  dependence in the data below the thermal conductivity maximum and since there were no obvious dips or other anomalies in the curve, all other scattering mechanisms, such as dislocation, resonant, dipole, etc., were initially disregarded. Using Equations [7], [9], [22], and [24], the resulting relaxation time has the form

$$\tau_c^{-1} = \frac{v}{L} + A \omega^4 + [B_1 \exp(-\theta/aT) + B_2] \omega^2 T \quad [47]$$

Equations [7] and [8] allow an estimation of the boundary scattering relaxation time,  $\tau_B$ . For example, the cross-sectional area dimensions for sample K2 were  $l_1 = 4.45$  mm and  $l_2 = 3.55$  mm. Using these in the equation

$$L = 2 \pi^{-\frac{1}{2}} (l_1 l_2)^{\frac{1}{2}} \quad [8]$$

the effective Casimir length,  $L$ , was 4.45 mm. From the elastic constants given by Gesland et al. (24) and using Equation [38-c], the average velocity of sound at room temperature was calculated to be  $3.74 \times 10^5$  cm/sec, giving  $\tau_B^{-1} = 8.40 \times 10^5 \text{ sec}^{-1}$ .

Point defect scattering relaxation time,  $\tau_{PD}$ , was estimated for the effect of isotopes by using Equations [9], [10], [12], [13], and [14]. Relating the form  $A_x B_y C_z$  to potassium zinc fluoride,  $x = 1$ ,  $y = 1$ ,  $z = 3$ ,

A = potassium, B = zinc, and C = fluoride. The approximation for the constant A of the equation

$$\tau_{PD}^{-1} = A \omega^2 \quad [9]$$

is given by the relation

$$A = \frac{\delta^3 \Gamma}{4\pi v^2} \quad [10]$$

which gives  $4.7 \times 10^{-46} \text{ sec}^3$ . The details of this calculation are given in Appendix A.

The relaxation time resulting from umklapp and normal phonon-phonon processes had the forms given in Equations [22] and [24] respectively

$$\tau_U^{-1} = B_1 T \omega^2 e^{-\theta/aT} \quad [22]$$

$$\tau_N^{-1} = B_2 T \omega^2 \quad [24]$$

The constants  $B_1$  and  $B_2$  were taken as fitted parameters. Fitting the high temperature data, the values obtained were  $7 \times 10^{-18} \text{ sec/K}$  for  $B_1$  and  $7 \times 10^{-21} \text{ sec/K}$  for  $B_2$ .

The isotope point defect and phonon-phonon scattering effects depended primarily only on the compound being measured; therefore, the calculated and fitted relaxation times should be the same for all the present samples. However, the boundary scattering, important at low temperatures, should be entirely dependent on the size of the sample, resulting in a different value of L, the Casimir length, for each sample. Using the dimensions of the samples listed in Table I, the calculated Casimir lengths,

L, are given in Table VII. Since all the curves were essentially the same at low temperatures, a representative computer fit was obtained only for sample K2.

The curve obtained using the values discussed above is given in plot 1 of Figure 14. At 2 K this curve was a factor of 33 larger than the experimental curve for K2, given in plot 2 of Figure 14 for comparison; and the peak region was a factor of 24 larger. Assuming the possibility of a larger number of point defects than those resulting from the isotopes only, A was adjusted to give the best fit, although while keeping the constants for the boundary term, L, and phonon-phonon terms,  $B_1$  and  $B_2$ , constant, a reasonable fit of the data could not be obtained. However, when A was increased to  $1 \times 10^{-43} \text{ sec}^3$ , there was only a factor of 6 difference between the two curves at 8 K, but at 2 K a factor of 25 remained. This is plot 3 of Figure 14.

The calculated value for the boundary scattering term should be the most reliable calculated constant since the size of the samples and the velocity of sound values in the material can be measured with confidence. Maintaining the value for L of 4.45 mm, an attempt was made to obtain a reasonable fit of the experimental data by taking all possible combinations of the point defect, umklapp, normal, dislocation, and dipole scatterings. However, no reasonably close fit could be obtained.

Even though the measured low temperature thermal con-

TABLE VII  
CALCULATED CASIMIR LENGTHS FOR THE SAMPLES

Sample	Casimir Lengths $L = 2\pi^{-\frac{1}{2}}(l_1 l_2)^{\frac{1}{2}}$
K1 undoped	3.29 mm
K2 undoped	4.45 mm
K3 undoped	3.07 mm
KN1 Ni-doped	3.24 mm
KN2 Ni-doped	4.17 mm



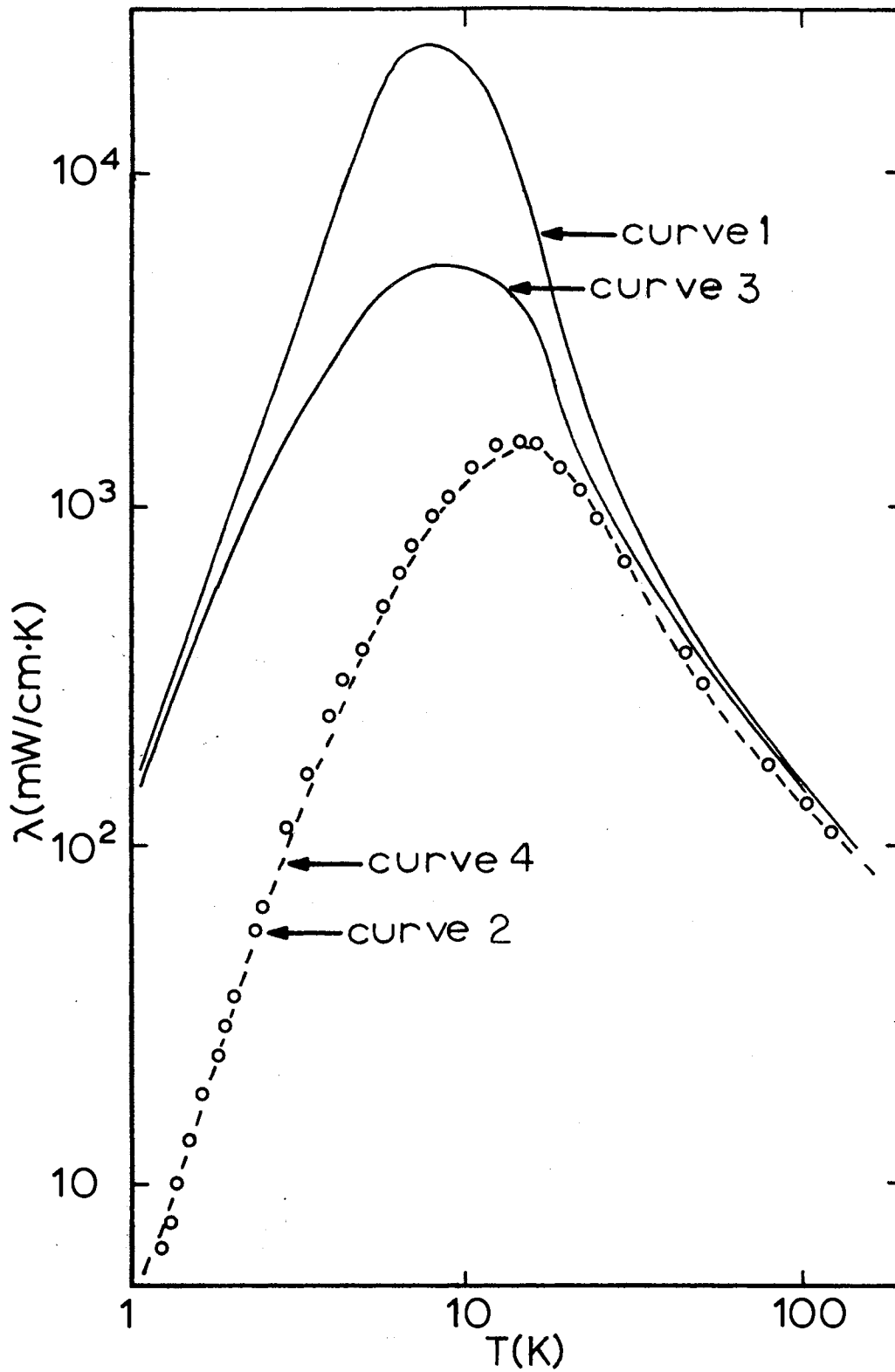


Figure 14. Theoretical Curves of Potassium Zinc Fluoride Calculated by the Debye-Callaway Theory

ductivity had the correct temperature dependence in the  $T^3$  region, it was a factor of 25 lower than the theoretical low temperature thermal conductivity calculated using the theoretical Casimir length. Only by adjusting  $L$  to 0.14 mm could a good fit be obtained as is shown in plot 4 of Figure 14. This value is  $3.1 \times 10^{-2}$  times smaller than the measured value. The fitted and calculated parameters for the curves of Figure 14 are given in Table VIII.

This type of effect, where the measured thermal conductivity in the boundary dominant region has the  $T^3$  temperature dependence but not the correct boundary size value, had been observed by a number of authors (50, 56, 63, 72, 93, 94, 95). None of these authors treated this problem rigorously but only hinted as to what he believed to be the scattering mechanisms. In the related compound potassium magnesium fluoride, which has physical and chemical properties very similar to those of potassium zinc fluoride, Harley and Rosenberg (93) had experimental values of  $L$  for four nickel-doped samples of potassium magnesium fluoride which were "less by a factor of 2 to 5 than the smallest dimension" of their samples. Figure 13 shows their experimental results for potassium magnesium fluoride: 0.5 percent nickel and 3.0 percent nickel. Their only explanation for having to reduce their Casimir length to obtain a reasonable fit to the data was that the crystals contained some "macroscopic defect." Other authors gave possibilities of grain boundaries, clusters,

TABLE VIII  
PARAMETERS USED IN THE DEBYE-CALLAWAY INTEGRAL

Curve #	L (mm)	A (sec <sup>3</sup> )	B <sub>1</sub> (sec/deg)	B <sub>2</sub> (sec/deg)
1	4.45	$4.7 \times 10^{-46}$	$7 \times 10^{-18}$	$7 \times 10^{-21}$
2	Experimental Data: Sample K2			
3	4.45	$1 \times 10^{-43}$	$7 \times 10^{-18}$	$7 \times 10^{-21}$
4	0.14	$1 \times 10^{-43}$	$7 \times 10^{-18}$	$7 \times 10^{-21}$

colloids, bubbles, and magnetic impurities. Although grain boundaries and clusters could not be ruled out in the present study, they were not considered likely to be the scattering mechanisms reducing the Casimir length. Formation of colloids was a strong possibility; however, there was no method of testing for them except to note that a similar effect as that described in the next section about the laser experiment would indicate the possibility of their presence.

Visual examination of the boules from which the samples were cut showed that each boule contained bubbles to varying degrees. The samples were cut to minimize the number of bubbles in each one. Sample K1 had some large bubbles in its center; K2 had many bubbles in its bottom portion where the gradient heater was wound but appeared to have only a few small ones between the thermometer clamps; and K3 had a few small bubbles in its bottom portion but none between the thermometer clamps. The nickel-doped samples, KN1 and KN2, appeared to have no bubbles although there were some in other parts of the boule. By shining a helium laser with a beam of  $6328\text{\AA}$  through the sample, it appeared that some light was scattered, which may have been the result of small bubbles. From the low temperature thermal conductivity data, for these bubbles to scatter as boundaries, they must be on an average of 0.14 mm apart and must have a diameter greater than  $400\text{\AA}$  because the mean-free-path was approximately 0.14 mm and the dominant phonon

wavelength was approximately  $400\text{\AA}$ . Since all the samples contained bubbles of varying sizes and densities, the bubbles might have been causing the effect of a small constant mean-free-path.

The specifications of the crystal-growing materials and an analysis of the potassium zinc fluoride showed a number of magnetic impurities, such as iron, chromium, vanadium, and nickel, which indicated that there might have been some type of resonance scattering as a result of magnetic impurities. Nickel impurities of the percentages present may have had a small effect on the zero field thermal conductivity as can be seen by comparing the low temperature data of samples K2 and KN2. This can be seen in Figure 15, which shows a plot of  $\lambda/T^3$  versus  $T$  between 0.5 to 5 K. Note that between 1.5 and 4.5 K, undoped potassium zinc fluoride, K2, had a  $T^3$  dependence; however, for this same region the nickel-doped sample, KN2, had a temperature dependence slightly larger than  $T^3$ , and for temperatures below 1.5 K it had a temperature dependence less than  $T^3$ . Harley and Rosenberg (93) noted an increase in the temperature dependence for zero fields as nickel concentrations increased; however, at low temperatures they did not see a changing of the slope to less than  $T^3$  as in this study. These data are shown in Figure 13. Vanadium has not been previously reported as causing a drastic drop in the zero field thermal conductivities of similar types of materials. Chromium has been reported in one paper (96) to have caused

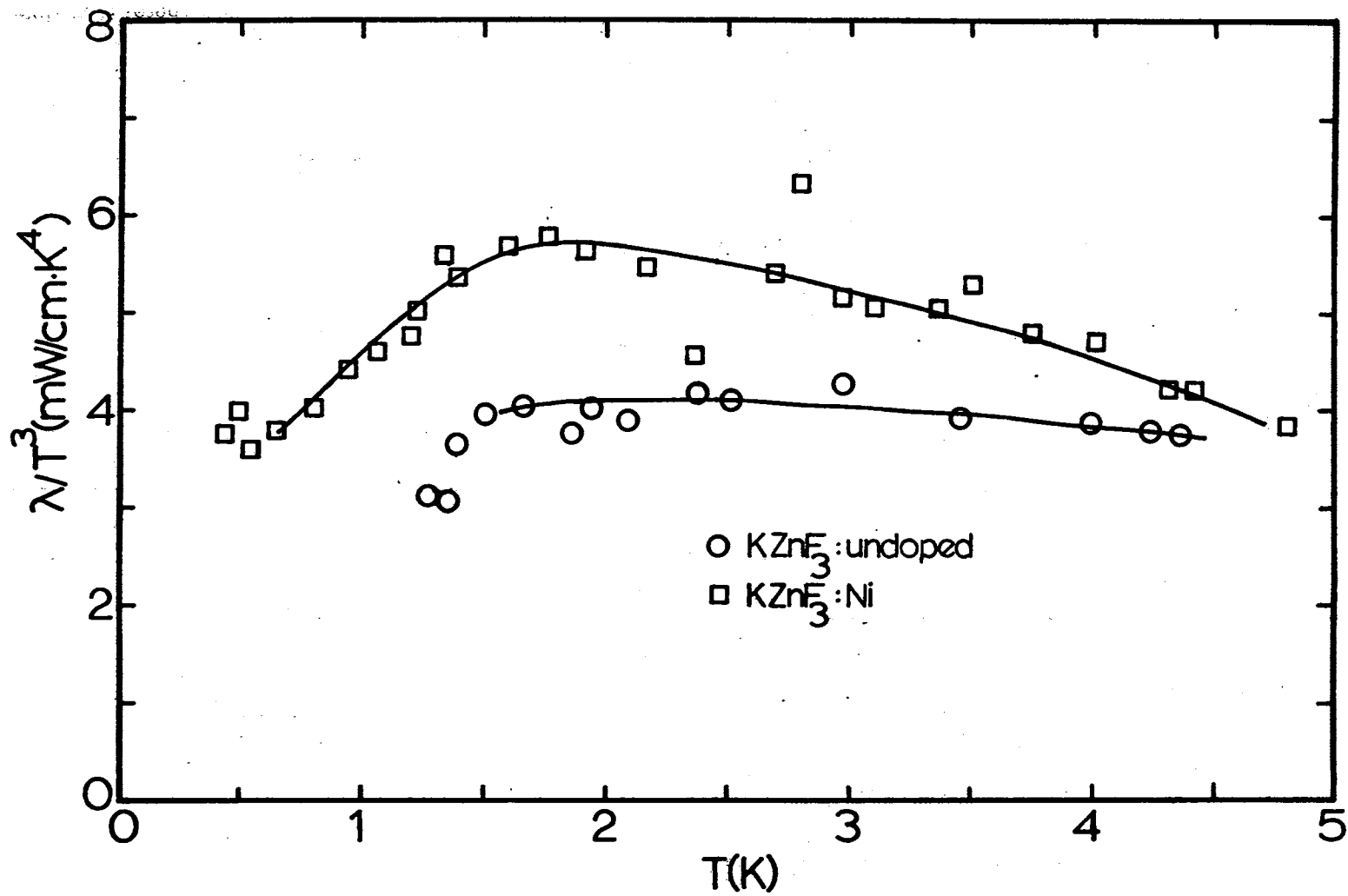


Figure 15. Plot of  $\lambda/T^3$  vs. T

a marked drop in the low temperature thermal conductivity of magnesium oxide but in concentrations of the order of 3,000 parts per million, whereas in these samples it was less than one part per million. On the other hand, numerous authors (45, 55, 63, 70, 71, 97, 98, 99) have noted a drastic drop in the zero field thermal conductivities of various substances containing small quantities of iron, in one case with only one part per million. Most of these data were for the thermal conductivity of magnesium oxide, and the drop in most cases occurred above the peak region. Because of the crystal field splittings of iron (Appendix G) and chromium, which have many low-lying levels separated by energy differences of the same order of magnitude as those of the thermal phonons, a strong possibility exists that there is magnetic scattering which may result in a  $T^3$  dependence. Two possible forms of the relaxation time are given in Equations [33] and [34]. However, detailed knowledge of the level diagram of each of these paramagnetic metals in the octahedral crystal field of potassium zinc fluoride is required to make more definite statements as to their effect on the low temperature thermal conductivity. Energy level diagrams for the 3d transition metals iron and nickel found in the samples are presented in Appendixes G and H.

#### Summary

The thermal conductivities of three undoped and two

nickel-doped samples of potassium zinc fluoride were measured over the large temperature range from 0.42 to 200 K. The results were analyzed in terms of the Debye-Callaway model with boundary, isotope, and phonon-phonon scattering rates. It was necessary to increase the point defect term as isotope scattering alone did not account for the height of the peak. More important, however, was that the calculated Casimir mean-free-path was a factor of 25 larger than that required to fit the data for all the samples. This suggested that another scattering mechanism, such as bubbles acting as boundaries or resonant scattering from paramagnetic impurities, must be included. With the information available, neither the particular scattering mechanism nor the form of the relaxation time could be determined.

#### Future Work

In order to determine if magnetic scattering by paramagnetic impurities can be included as a possible scattering mechanism, the low temperature thermal conductivities of the undoped sample K2 should be extended to lower temperatures and they should be taken as a function of the magnetic field. Preliminary measurements of the magnetic field dependence of the low temperature thermal conductivities of KN2 have been made indicating that the thermal conductivity does depend on the field; however, this is what is expected because of the nickel doping.



More measurements should be taken to determine the field dependence of potassium zinc fluoride with dilute nickel doping. To completely interpret the present results, an undoped sample of potassium zinc fluoride that does not contain paramagnetic impurities or bubbles must be measured. Then an iron-doped sample and a chromium-doped sample should be measured.

## BIBLIOGRAPHY

1. D. S. Crocket and H. M. Haendler, *J. Am. Chem. Soc.* 82, 4158 (1960).
2. K. Knox, *Acta Cryst.* 14, 583 (1961).
3. J. Ferguson and H. J. Guggenheim, *J. Chem. Phys.* 44, 1095 (1966).
4. R. L. Martin, R. S. Nyholm, and N. C. Stephenson, *Chemistry and Industry*, 83 (1956).
5. H. Swanson, N. T. Gilfrich, and G. M Ugrinic, *Natl. Bur. Standards Circ.* 5, 51 (1955).
6. R. C. DeVries and R. Roy, *J. Am. Chem. Soc.* 75, 2479 (1953).
7. I. Mockrin, U. S. patent number 2,899,321.
8. I. Nakagawa, A. Tsuchida, and T. Shimanouchi, *J. Chem. Phys.* 47, 982 (1967).
9. V. O. Schmitz-DuMont and H. Bornefeld, *Z. Anorg. u. Allgem. Chem.* 287, 120 (1956).
10. H. A. Klasens, P. Zalm, and F. O. Huysman, *Philips Res. Rep.* 8, 441 (1953).
11. W. L. W. Ludekens and A. J. E. Welch, *Acta Cryst.* 5, 841 (1952).
12. A. L. Smith, *J. Electrochem. Soc.* 101, 189 (1954).
13. M. M. Abraham, C. B. Finch, J. L. Kolopus, and J. T. Lewis, *Phys. Rev. B.* 3, 2855 (1971).
14. B. V. Beznosikov and N. V. Beznosikova, *Soviet Physics - Crystallography* 13, 158 (1968).
15. D. J. Breed, K. Giligamse, J. W. E. Sterkenburg, and A. R. Miedema, *J. Appl. Phys.* 41, 1267 (1970).
16. R. B. Frankel, J. Chappert, J. R. Regnard, A. Misetich, and C. R. Abeledo, *Phys. Rev. B.* 5, 2469 (1972).

17. K. Gesi, J. D. Axe, G. Shirane, and A. Linz, Phys. Rev. B. 5, 1933 (1972).
18. H. Guggenheim, J. Phys. Chem. 64, 938 (1960).
19. T. P. P. Hall, W. Hayes, R. W. H. Stevenson, and J. Wilkens, J. Chem. Phys. 38, 1977 (1963).
20. R. Roy, J. Am. Ceram. Soc. 37, 581 (1954).
21. S. Ogawa, J. Phys. Soc. Japan 15, 1475 (1960).
22. B. M. Wanklyn, J. Inorg. and Nucl. Chem. 27, 481 (1965).
23. Y. Yamaguchi and N. Sakamoto, J. Phys. Soc. Japan 27, 1444 (1969).
24. J. Gesland, M. Binois, and J. Nouet, C. R. Acad. Sc. Paris 275, 551 (1972).
25. E. W. Prohofskey, W. W. Holloway, Jr., and M. Kestigian, J. Appl. Phys. 36, 1041 (1965).
26. J. Ferguson, H. J. Guggenheim, and Y. Tanabe, J. Appl. Phys. 36, 1046 (1965).
27. R. Stevenson, Phys. Rev. 152, 531 (1966).
28. N. Sakamoto and Y. Yamaguchi, J. Phys. Soc. Japan 22, 885 (1967).
29. M. D. Sturge, Phys. Rev. B. 1, 1005 (1970).
30. T. P. P. Hall and A. Leggeat, Solid State Commun. 7, 1657 (1969).
31. C. R. Riley and W. A. Sibley, Phys. Rev. B. 1, 2789 (1970).
32. W. E. Vehse and W. A. Sibley, Phys. Rev. B. 6, 2443 (1972).
33. C. R. Riley, S. I. Yun, and W. A. Sibley, Phys. Rev. B. 5, 3285 (1972).
34. L. A. Kappers and L. E. Halliburton (to be published in J. Phys. C.).
35. A. P. Lane, D. W. A. Sharp, J. M. Barraclough, D. H. Brown, and D. A. Paterson, J. Chem. Soc. (A) 1, 94 (1971).

36. P. G. Klemens, Solid State Physics, 7, 1 (1958),  
edited by F. Seitz and D. Turnbull (Academic  
Press, New York).
37. P. G. Klemens, Encyclopedia of Physics, 14, 198 (1956),  
edited by S. Flugge (Springer-Verlog, Berlin).
38. P. Carruthers, Rev. Mod. Phys. 33, 92 (1961).
39. P. Debye, Vorträge Überdie Kinetische Theorie der  
Materie and der Electricität, 1914.
40. R. E. Peierls, Ann. Physik, 3, 1055 (1929).
41. P. G. Klemens, Proc. Phys. Soc. 68, 1113 (1955).
42. P. G. Klemens, Proc. Roy. Soc. A208, 108 (1951).
43. J. M. Ziman, Electrons and Phonons (Clarendon Press,  
Oxford, 1960).
44. R. E. Peierls, Quantum Theory of Solids (Clarendon  
Press, Oxford, 1955).
45. J. Callaway, Phys. Rev. 113, 1046 (1959).
46. H. B. G. Casimir, Physica 5, 495 (1938).
47. R. Berman, E. L. Foster, and J. M. Ziman, Proc. Roy.  
Soc. A231, 130 (1955).
48. G. A. Slack, Phys. Rev. 105, 832 (1957).
49. R. Berman, F. E. Simon, and J. M. Ziman, Proc. Roy.  
Soc. A220, 171 (1953).
50. M. G. Holland and L. J. Neuringer, Proc. Internatl.  
Conf. on Physics of Semiconductors, 474 (1962).
51. D. Walton, Phys. Rev. 135, A753 (1964).
52. J. M. Worlock, Phys. Rev. 147, 636 (1966).
53. R. O. Pohl, Phys. Rev. 118, 1499 (1960).
54. J. A. Carruthers, J. F. Cochran, and K. Mendelssohn,  
Cryogenics 2, 160 (1962).
55. D. Walton, Phys. Rev. B. 1, 1234 (1970).
56. D. L. Huber, Phys. Lett. 20, 230 (1966).
57. C. T. Walker and R. O. Pohl, Phys. Rev. 131, 1433  
(1963).

58. E. F. Steigmeier, Thermal Conductivity, 2, 203 (1969), edited by R. P. Tye (New York).
59. I. Pomeranchuk, J. Phys. (U.S.S.R.) 4, 259 (1941).  
[Original not available; cited in Reference 36.]
60. M. V. Klein, Phys. Rev. 141, 716 (1966).
61. G. A. Slack, Phys. Rev. 126, 427 (1962).
62. R. Berman and J. C. F. Brock, Proc. Roy. Soc. A289, 46 (1966).
63. G. A. Slack and S. Galginaitis, Phys. Rev. 133, A253 (1964).
64. P. D. Tacher, Phys. Rev. 156, 975 (1967).
65. C. Herring, Phys. Rev. 95, 954 (1954).
66. M. G. Holland, Phys. Rev. 132, 2461 (1963).
67. K. Ohashi, J. Phys. Soc. Japan 24, 437 (1968).
68. R. O. Pohl, Phys. Rev. Lett. 8, 481 (1962).
69. R. Orbach, Phys. Rev. Lett. 8, 393 (1962).
70. I. P. Morton and M. F. Lewis, Phys. Rev. B. 3, 552 (1971).
71. G. T. Fox, M. W. Wolfmeyer, J. R. Dillinger, and D. L. Huber, Phys. Rev. 165, 898 (1968).
72. G. T. Fox, M. W. Wolfmeyer, J. R. Dillinger, and D. L. Huber, Phys. Rev. 181, 1308 (1969).
73. R. Orbach, Proc. Roy. Soc. A298, 357 (1967).
74. M. Moss, J. Appl. Phys. 36, 3308 (1965).
75. G. Leibfried and E. Schlömann, Nachr. Akad. Wiss. Goettingen, Math: physik Kl 11a, 71 (1954).  
[Original available but not translated; translation secured from U. S. Atomic Energy Commission Report AEC-tr-5892.]
76. C. L. Julian, Phys. Rev. 137, A128 (1965).
77. E. F. Steigmeier and I. Kudman, The Fifth Conference on Thermal Conductivity 1, III-C-1 (1965).
78. M. Roufosse and P. G. Klemens, Phys. Rev. B. 7, 5379 (1973).

79. P. W. Bridgman, Proc. Am. Acad. Arts and Sciences 60, 303 (1925).
80. D. C. Stockbarger, Rev. Sci. Instr. 7, 133 (1936).
81. D. C. Stockbarger, Disc. Faraday Soc. 5, 294 (1949).
82. C. T. Butler, (Unpub. M. S. thesis, Oklahoma State University, 1967.)
83. A. E. Whiteman, (Unpub. M. S. thesis, Oklahoma State University, 1970.)
84. P. P. Velasco. (Unpub. M. S. thesis, Oklahoma State University, 1973.)
85. J. J. Martin. (Unpub. Ph. D. thesis, Iowa State University, 1967.)
86. L. L. Sparks, R. L. Powell, and W. J. Hall, Natl. Bur. Stand. Rpt. 9712 (1968).
87. M. W. Wolf and J. J. Martin, Phys. Stat. Sol. 17, 215 (1973).
88. L. L. Sparks and R. L. Powell, J. of Reserach of the Natl. Bur. Standards 76A, 263 (1972).
89. D. K. Finnemore, Rev. Sci. Instr. 36, 1364 (1965).
90. A. C. Rose-Innes, Low Temperature Techniques (The English Universities Press Ltd., London, 1964).
91. M. C. Hetzler. (Unpub. Ph. D. thesis, Vanderbilt University, 1970.)
92. Y. Suemune and H. Ikawa, J. Phys. Soc. Japan 19, 1686 (1964).
93. R. T. Harley and H. M. Rosenberg, Proc. Roy. Soc. A315, 551 (1970).
94. G. A. Slack and D. W. Oliver, Phys. Rev. B. 4, 592 (1971).
95. M. G. Holland, Phys. Rev. 134, A471 (1964).
96. L. J. Challis, A. M. de Goër, K. Guckelsberger, and G. A. Slack, Proc. Roy. Soc. A330, 29 (1972).
97. G. T. Fox, M. W. Wolfmeyer, J. R. Dillinger, and D. L. Huber, Phys. Rev. 165, 898 (1968).

98. M. F. Lewis and I. P. Morton, Phys. Lett. 27A, 547  
(1968).
99. G. A. Slack, General Electric Report No. 66-C-481  
(1966).

APPENDIX A

THE CALCULATION OF THE PARAMETERS  $\Gamma$  OF  
EQUATION 12 FOR ISOTOPE POINT DEFECT  
SCATTERING IN  $\text{KZnF}_3$

$$\begin{aligned}\Gamma &= \frac{1}{5} \left( \frac{\bar{M}_K}{\bar{M}} \right)^2 \Gamma_K + \frac{1}{5} \left( \frac{\bar{M}_{Zn}}{\bar{M}} \right)^2 \Gamma_{Zn} + \frac{3}{5} \left( \frac{\bar{M}_F}{\bar{M}} \right)^2 \Gamma_F \\ &= \frac{1}{5} \left( \frac{39.1}{161} \right)^2 \Gamma_K + \frac{1}{5} \left( \frac{65.4}{161} \right)^2 \Gamma_{Zn} + \frac{3}{5} \left( \frac{19.0}{161} \right)^2 \Gamma_F \\ &= 3.71 \times 10^{-6}\end{aligned}$$

where

$$\begin{aligned}\Gamma_K &= \sum_i f_{Ki} \left( \frac{\Delta M_{Ki}}{\bar{M}_K} \right)^2 \quad \text{with } i = 39, 40, 41 \\ &= (0.931) \left( \frac{0.102}{39.0} \right)^2 + (1.18 \times 10^{-4}) \left( \frac{0.898}{40.0} \right)^2 + \\ &\quad (0.0688) \left( \frac{1.90}{41.0} \right)^2 = 1.54 \times 10^{-4} \\ \Gamma_{Zn} &= \sum_i f_{Zni} \left( \frac{\Delta M_{Zni}}{\bar{M}_{Zn}} \right)^2 \quad \text{with } i = 64, 66, 67, 68, 70 \\ &= (0.489) \left( \frac{1.37}{64} \right)^2 + (0.278) \left( \frac{0.63}{66} \right)^2 + (0.041) \left( \frac{1.63}{67} \right)^2 \\ &\quad + (0.186) \left( \frac{0.026}{68} \right)^2 + (6.2 \times 10^{-3}) \left( \frac{4.63}{70} \right)^2 \\ &= 5.79 \times 10^{-4}\end{aligned}$$



## APPENDIX A (continued)

$$\begin{aligned}\Gamma_F &= \sum_i f_{Fi} \left( \frac{\Delta M_{Fi}}{\bar{M}_F} \right)^2 && \text{with } i = 19 \\ &= (1.00) \left( \frac{1.6 \times 10^{-3}}{19} \right)^2 = 7.1 \times 10^{-9}\end{aligned}$$

APPENDIX B

TABULATION OF DATA FOR SAMPLE NUMBER K1

( $\text{KZnF}_3$ : UNDOPED)

3 to 200 K Apparatus - L/A = 4.65

<u>Temperature (K)</u>	<u>Thermal Conductivity (mW/cm·K)</u>	<u>Power Input (mW)</u>	<u><math>\Delta T</math> (mK)</u>
150.	96.1	13.4	648.
116.	129.	15.3	551.
101.	129.	13.1	472.
92.3	156.	15.3	457.
78.0	185.	15.3	383.
77.5	181.	2.47	63.4
77.5	180.	1.31	33.7
54.6	271.	16.1	276.
48.6	310.	9.25	139.
37.0	427.	19.8	216.
31.0	526.	19.7	114.
26.7	665.	19.6	137.
22.9	825.	19.5	111.
22.5	817.	18.1	103.
19.9	948.	19.5	95.4
18.8	996.	19.0	88.9
17.0	1060.	12.5	54.8
16.4	1090.	19.4	82.6
13.8	1090.	8.08	34.6
12.6	1030.	19.3	87.3
11.4	939.	4.20	20.8
9.32	842.	19.2	106.
8.59	753.	4.08	25.2
8.54	703.	19.7	130.
7.75	624.	16.8	125.
6.98	529.	26.1	229.
6.79	517.	19.7	177.
5.94	430.	19.2	207.
5.93	420.	19.7	218.
5.44	370.	12.6	159.
5.23	329.	8.84	125.
5.07	328.	7.75	110.
4.42	272.	3.06	52.3

APPENDIX C

TABULATION OF DATA FOR SAMPLE NUMBER K2

( $\text{KZnF}_3$ : UNDOPED)

3 to 200 K Apparatus - L/A = 5.22

<u>Temperature (K)</u>	<u>Thermal Conductivity (mW/cm<math>\cdot</math>K)</u>	<u>Power Input (mW)</u>	<u><math>\Delta T</math> (mK)</u>
297.	64.6	25.0	2017
103.	132.	32.4	1281
90.6	154.	37.8	1250
81.9	170.	31.2	957.
79.8	178.	11.4	335.
50.4	315.	26.1	433.
49.1	327.	11.2	179.
45.6	373.	9.72	136.
29.7	695.	32.3	243.
27.6	795.	34.3	225.
24.8	932.	32.1	180.
22.2	1120	21.7	101.
20.2	1270	32.0	131.
19.1	1320	16.0	63.6
18.1	1430	27.2	99.5
16.6	1580	10.7	35.4
16.2	1550	27.1	91.5
14.7	1580	27.0	89.6
13.2	1540	24.5	83.1
12.5	1520	24.5	84.4
11.0	1360	24.3	93.4
10.3	1300	15.6	62.8
9.06	1080	15.6	75.3
8.09	948.	15.6	85.8
7.08	761.	9.20	63.1
6.34	633.	17.1	141.
6.13	596.	15.5	136.
5.98	567.	13.2	122.
5.68	510.	9.75	99.7
5.22	419.	4.52	56.3
5.00	381.	2.30	31.5

## APPENDIX C (continued)

1.2 to 4 K Apparatus -  $L/A = 6.50$ 

<u>Temperature (K)</u>	<u>Thermal Conductivity (mW/cm·K)</u>	<u>Power Input (mW)</u>	<u><math>\Delta T</math> (mK)</u>
4.35	312.	4.51	94.0
4.23	286.	4.63	105.
3.98	244.	4.63	123.
3.47	163.	2.31	91.9
2.98	113.	2.31	133.
2.52	65.6	.846	83.8
2.40	57.9	.885	99.4
2.11	36.3	.325	63.0
1.95	29.6	.363	79.7
1.86	24.3	.236	63.4
1.66	18.4	.259	91.2
1.51	13.4	.177	85.5
1.40	10.0	.109	70.8
1.36	7.71	.330	27.9
1.28	6.54	.330	32.8

## APPENDIX D

## TABULATION OF DATA FOR SAMPLE NUMBER K3

(KZnF<sub>3</sub>: UNDOPED)

3 to 200 K Apparatus - L/A = 8.48

<u>Temperature (K)</u>	<u>Thermal Conductivity (mW/cm·K)</u>	<u>Power Input (mW)</u>	<u>ΔT (mK)</u>
301.	75.2	25.9	2920
190.	80.0	16.0	1690
174.	86.4	17.9	1760
156.	91.0	10.6	995.
140.	101.	18.1	1520
121.	114.	17.9	1330
121.	112.	11.2	842.
110.	126.	18.0	1210
102.	133.	16.0	1024
101.	133.	26.1	1670
94.6	143.	26.8	1590
90.3	150.	15.8	889.
89.0	151.	6.60	371.
85.8	159.	26.0	1380
84.4	163.	22.8	1190
78.7	182.	22.5	1050
78.4	171.	15.8	782.
74.2	182.	25.7	1200
68.0	204.	25.4	1060
62.9	220.	28.1	1080
56.4	243.	27.1	947.
51.3	269.	25.7	809.
45.5	315.	7.25	195.
40.3	349.	25.9	630.
34.7	413.	25.6	526.
31.2	490.	24.5	424.
28.6	519.	25.5	417.
26.3	617.	25.5	351.
24.0	669.	24.6	312.
21.2	792.	25.2	270.
20.1	844.	24.1	242.
18.5	925.	25.0	229.
17.5	983.	25.8	223.

## APPENDIX D (continued)

<u>Temperature (K)</u>	<u>Thermal Conductivity (mW/cm·K)</u>	<u>Power Input (mW)</u>	<u><math>\Delta T</math> (mK)</u>
16.6	1020	22.6	188.
15.2	1030	18.7	154.
13.9	1090	15.2	118.
13.9	1060	25.4	203.
13.3	1070	25.4	201.
13.1	969.	12.9	113.
12.2	998.	25.3	215.
11.4	994.	25.2	215.
10.3	927.	8.19	74.9
9.77	885.	6.43	61.6
9.24	845.	5.13	51.5
8.68	807.	3.92	41.2
8.33	740.	25.1	288.
7.78	663.	25.2	322.
7.16	607.	24.5	343.
6.86	578.	21.1	310.
6.21	508.	25.8	431.
5.68	434.	16.1	314.
5.24	373.	9.01	205.
5.23	382.	23.8	527.
4.86	335.	3.27	82.6
4.65	332.	.603	15.4
4.39	258.	12.1	397.
4.13	209.	6.43	261.
3.62	181.	5.58	261.
3.07	110.	2.41	185.
3.35	160.	9.42	500.
3.23	145.	7.78	456.
3.20	144.	7.80	460.
2.75	82.1	1.71	177.
2.64	76.4	1.96	217.

APPENDIX E

TABULATION OF DATA FOR SAMPLE NUMBER KN1

( $\text{KZnF}_3$ : \* NICKEL DOPED)

3 to 200 K Apparatus - L/A = 4.78

<u>Temperature (K)</u>	<u>Thermal Conductivity (mW/cm·K)</u>	<u>Power Input (mW)</u>	<u><math>\Delta T</math> (mK)</u>
195.	79.0	30.3	1840
147.	94.8	29.8	1500
126.	110.	38.1	1650
111.	124.	38.4	1480
99.0	141.	38.9	1324
93.8	146.	30.8	1010
90.5	158.	39.8	1201
81.1	173.	50.1	1390
79.1	176.	30.1	822.
66.5	213.	30.4	681.
49.2	319.	29.1	435.
41.1	379.	48.8	615.
35.1	477.	48.6	488.
29.2	623.	48.3	371.
25.1	779.	44.6	274.
22.4	905.	36.9	195.
19.9	937.	28.8	147.
19.6	1074	29.2	130.
18.1	1200	33.2	132.
16.7	1350	28.6	101.
14.7	1440	22.0	73.0
13.2	1440	17.1	56.9
12.6	1322	36.2	131.
11.8	1310	26.9	98.4
11.5	1300	42.7	157.
10.9	1290	46.3	171.
10.4	1210	32.1	127.
9.94	1160	46.2	191.
9.28	1110	48.5	208.
9.20	1050	42.6	194.
8.84	1050	44.2	201.
8.52	1020	47.8	225.
7.77	898.	34.5	183.

## APPENDIX E (continued)

<u>Temperature (K)</u>	<u>Thermal Conductivity (mW/cm·K)</u>	<u>Power Input (mW)</u>	<u>ΔT (mK)</u>
7.48	863.	46.5	258.
7.25	777.	48.1	296.
7.16	809.	46.5	275.
6.75	736.	39.7	258.
6.34	665.	31.3	225.
5.83	601.	20.6	164.
5.34	523.	12.3	113.
5.32	547.	12.1	106.
4.98	434.	24.3	268.
4.95	400.	9.38	112.
4.80	401.	9.40	112.
4.54	375.	11.2	143.
4.18	307.	10.3	160.
3.70	222.	8.43	182.
3.29	178.	3.86	104.
3.02	132.	2.72	99.1
2.79	103.	1.51	70.1
2.61	83.7	1.08	61.5
2.42	70.0	1.61	111.
2.26	59.4	.903	72.7



APPENDIX F

TABULATION OF DATA FOR SAMPLE NUMBER KN2

(KZnF<sub>3</sub>: NICKEL DOPED)

3 to 200 K Apparatus - L/A = 6.33

<u>Temperature (K)</u>	<u>Thermal Conductivity (mW/cm·K)</u>	<u>Power Input (mW)</u>	<u>ΔT (mK)</u>
274.	723.	13.3	1150
183.	78.9	30.0	2410
160.	90.6	30.4	2110
121.	111.	19.1	1080
103.	132.	21.2	1020
86.1	158.	47.4	1900
79.8	173.	47.5	1740
70.2	197.	49.3	1580
59.6	239.	44.0	1170
50.1	291.	29.1	633.
45.6	327.	50.2	973.
39.8	396.	50.1	801.
35.3	473.	50.1	670.
30.4	587.	49.7	536.
26.6	717.	49.6	438.
22.9	931.	49.4	336.
20.2	1130	46.6	260.
18.2	1240	45.6	232.
16.3	1370	37.0	171.
15.4	1410	32.2	144.
14.3	1460	46.1	199.
13.9	1450	43.8	191.
13.4	1470	46.4	200.
12.8	1410	36.6	165.
12.2	1400	33.5	151.
11.8	1400	31.6	143.
11.2	1380	43.3	199.
10.6	1320	47.1	226.
9.98	1280	44.1	218.
9.50	1200	46.1	243.
9.07	1170	45.7	248.
8.57	1080	44.2	259.
8.15	1010	46.6	291.

## APPENDIX F (continued)

<u>Temperature (K)</u>	<u>Thermal Conductivity (mW/cm·K)</u>	<u>Power Input (mW)</u>	<u><math>\Delta T</math> (mK)</u>
7.55	906.	35.6	249.
7.17	852.	47.9	356.
7.15	851.	47.9	356.
6.77	807.	38.9	305.
6.43	727.	31.2	272.
6.06	657.	26.8	258.
5.76	572.	19.0	210.
5.26	529.	29.1	348.
5.22	473.	10.6	142.
4.81	435.	19.6	286.
4.42	366.	17.5	303.
4.32	339.	12.3	229.
4.03	309.	12.5	255.
3.74	251.	9.36	236.
3.38	195.	6.23	202.
3.10	150.	3.67	155.
2.97	135.	3.03	142.
2.70	107.	1.52	89.9

1.2 to 4 K Apparatus - L/A = 6.18

3.51	229.
2.81	141.
2.38	61.8
2.37	61.4
2.17	55.9
1.92	40.1
1.77	32.8
1.60	23.3
1.40	14.7
1.33	13.2
1.23	9.16
1.21	8.52
1.21	8.24
1.20	7.88

0.42 to 1.5 K Apparatus - L/A = 4.136

1.32	9.59
1.20	7.44
1.06	5.49
0.939	3.63
0.822	2.26

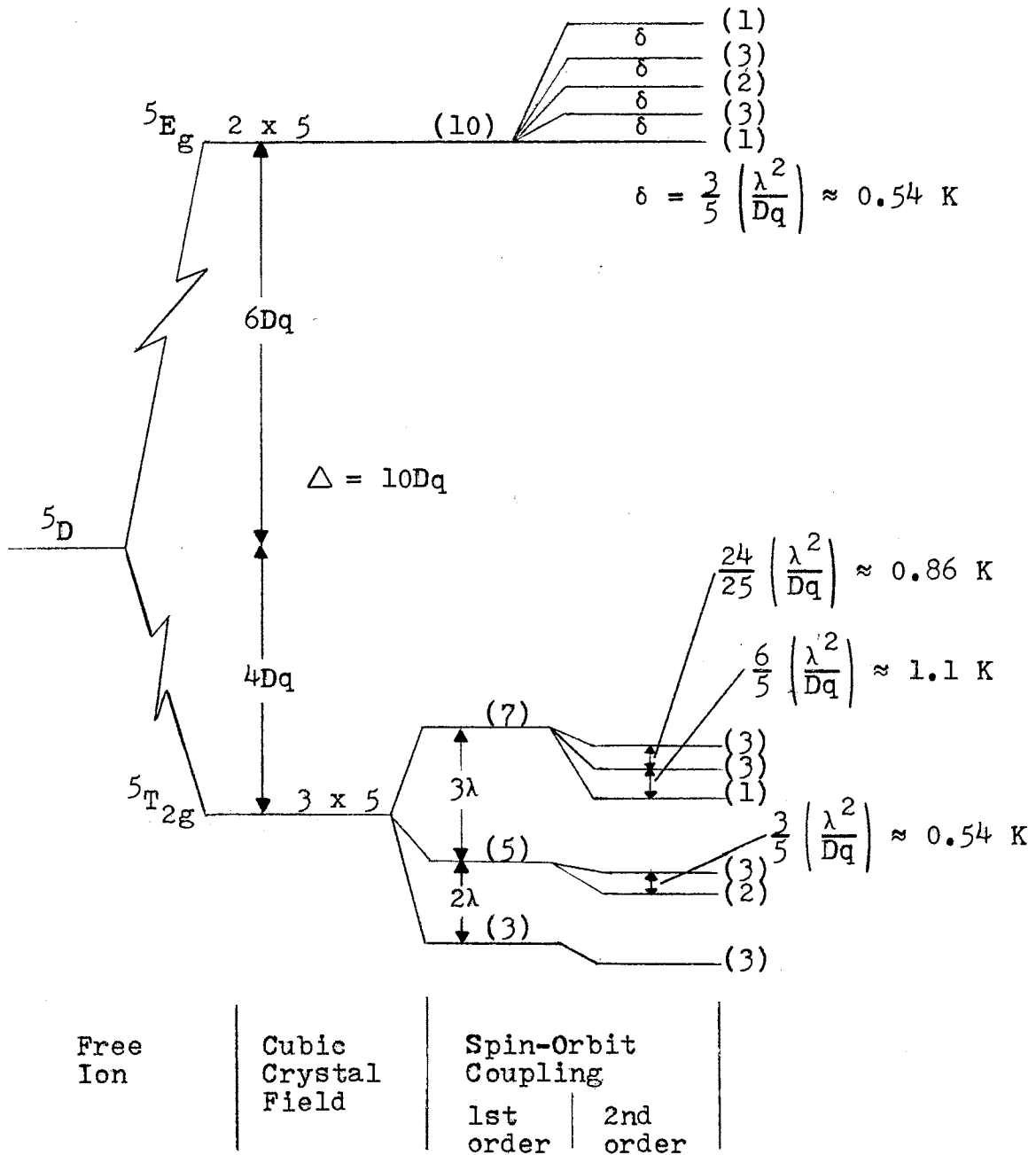
## APPENDIX F (continued)

<u>Temperature (K)</u>	<u>Thermal Conductivity (mW.cm.K)</u>
0.800	2.67
0.775	1.95
0.764	1.96
0.716	1.71
0.625	1.01
0.545	0.601
0.499	0.491
0.425	0.399
0.314	0.488

APPENDIX G

ENERGY LEVEL DIAGRAM FOR  $\text{Fe}^{2+} (3d^6)$

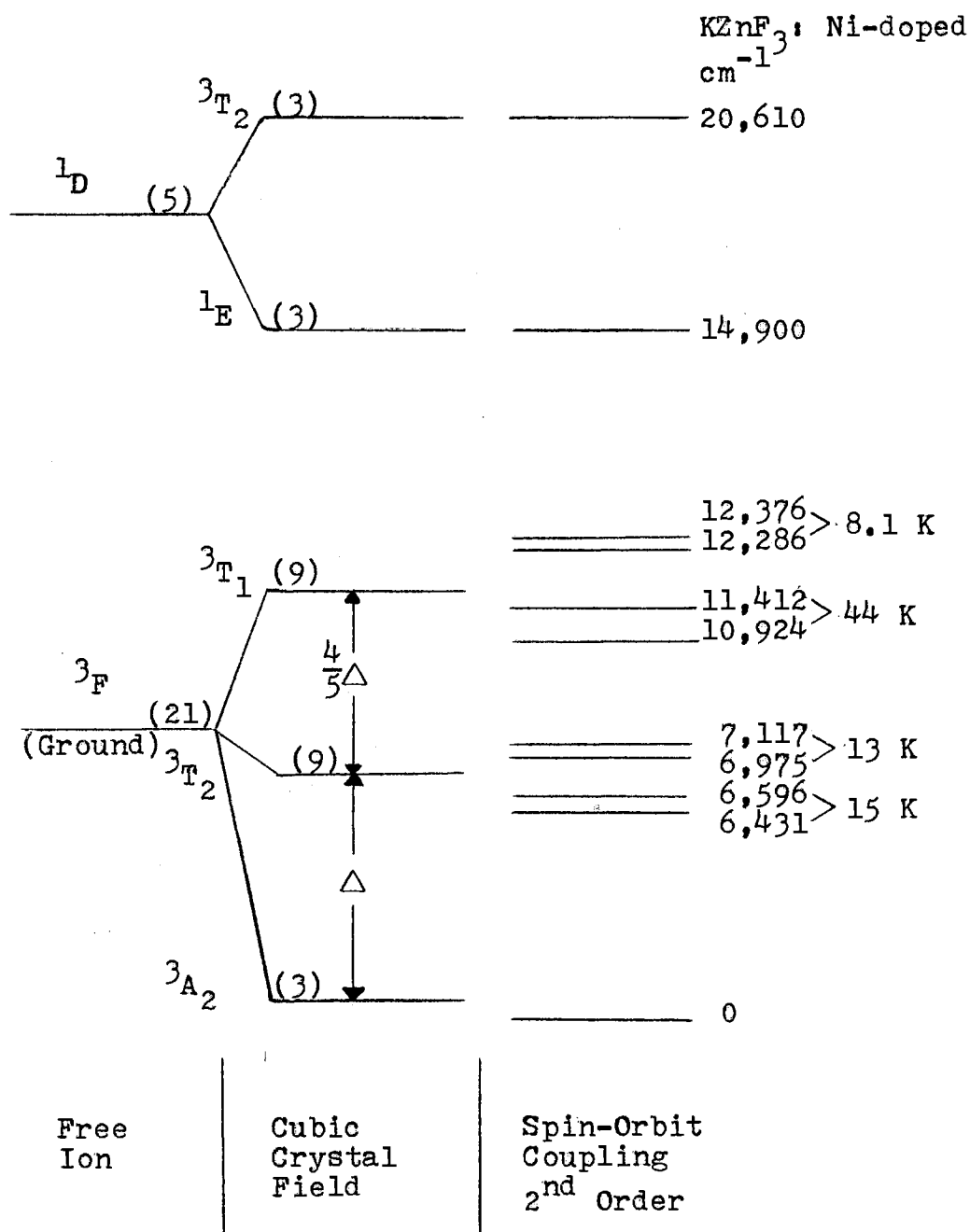
IN AN OCTAHEDRAL FIELD



APPENDIX H

ENERGY LEVEL DIAGRAM FOR  $\text{Ni}^{2+} (3d^8)$

IN AN OCTAHEDRAL FIELD



VITA

Michael Wayne Wolf

Candidate for the Degree of  
Doctor of Philosophy

Thesis: THE LOW TEMPERATURE THERMAL CONDUCTIVITY OF  
POTASSIUM ZINC FLUORIDE

Major Field: Physics

Biographical:

Personal Data: Born in Chicago, Illinois, May 7,  
1941, the son of Mr. and Mrs. W. M. Wolf.

Education: Graduated from Ela Vernon High School,  
Lake Zurich, Illinois, in June, 1960; received  
Bachelor of Science degree in Physics,  
Chemistry, and Mathematics from Carroll  
College in 1964; received Master of Science  
degree in Physics from Northern Illinois  
University in 1967; completed requirements  
for the Doctor of Philosophy degree at  
Oklahoma State University in July, 1974.

Professional Experience: Instructor at DeVry  
Institute of Technology, January-July, 1967;  
Instructor in the Physics Department at  
Indiana State University, 1967-69; Graduate  
Teaching Assistant in the Physics Department  
at Oklahoma State University, 1969-73;  
Instructor at Seminole Junior College, 1973-74.

Organizations: Member of Sigma Pi Sigma, American  
Association of Physics Teachers, Higher  
Education Alumni Council of Oklahoma, and  
Oklahoma Association of Community and Junior  
Colleges.